ANALYTICAL AND EXPERIMENTAL EVALUATION OF STIFFNESS PARAMETERS OF VOIDED CONCRETE SLAB BRIDGE

REPORT NO. 4 Final Progress Report

By: LARRY OLINE, Ph.D. & RAJAN SEN, Ph.D.
UNIVERSITY OF SOUTH FLORIDA
TAMPA, FLORIDA 99700-7369-119

For: FLORIDA DEPARTMENT 0'F TRANSPORTATION
SEPTEMBER, 1987

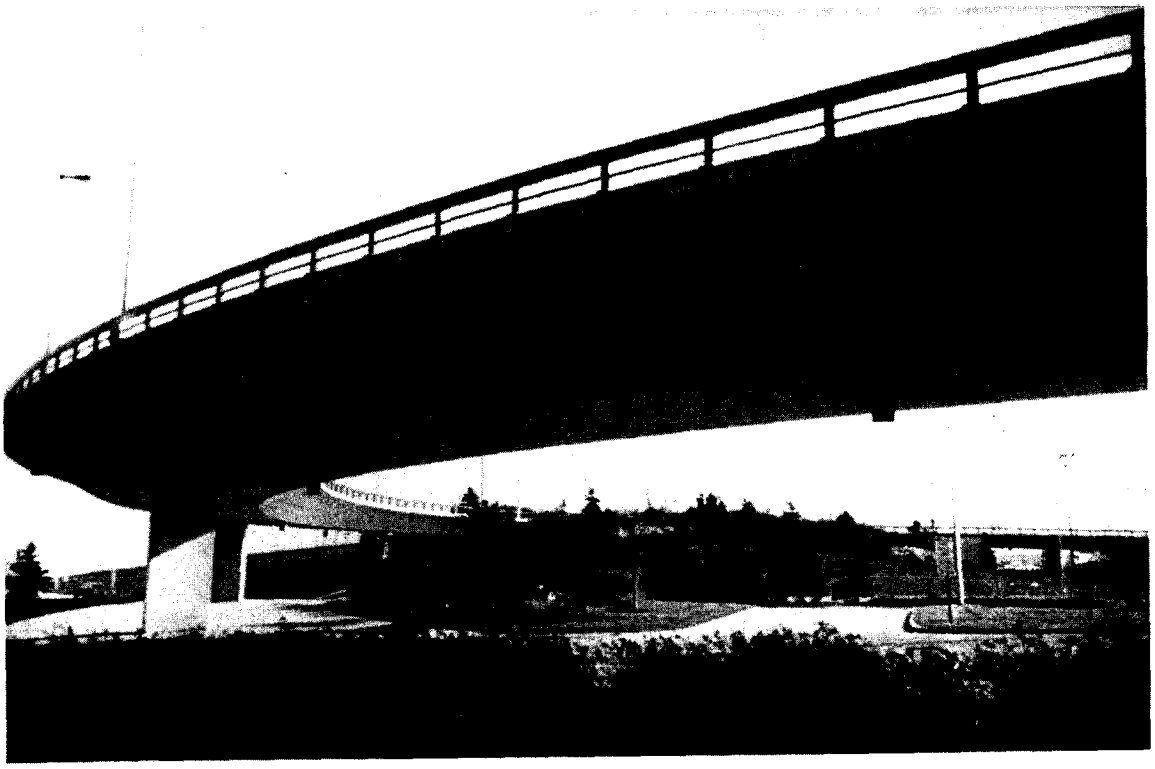

CIVIL ENGINEERING & MECHANICS

COLLEGE OF ENGINEERING
UNIVERSITY OF SOUTH FLORIDA

TABLE OF CONTENTS

1. INTRODUCTION

This is the fourth and final progress report on the FDOT contract entitled "Analytical and Experimental Evaluation of Stiffness Parameters of Voided Concrete Slab Bridges" and covers the period from June to October 1987.

The investigations related to ultimate strength are presented in Sections 2-5 and those related to three dimensional finite element analysis in the subsequent chapters.

2. ULTIMATE MOMENT CAPACITY OF LONGITUDINALLY & TRANSVERSELY PRESTRESSED SECTIONS

The third report contained results of preliminary investigations on the effect of the stress ratio a [transverse to longitudinal stress], on the uniaxial moment capacity. This report presents additional results of studies on rectangular, flanged and voided sections.

A description of the parametric studies conducted and the main conclusions are outlined in Sections 2.1 and 2.2. The application of the analysis to determine the ultimate moment capacity of voided sections is presented in Section 2.3. A discussion on the estimation of the stress ratio parameter a is contained in Section 2.4.

2.1 Parametric Studies

Since the ultimate behavior of a voided slab may be approximated either by a rectangular or a flanged section the parametric studies conducted examined only rectangular and flanged sections.

The results of the investigation presented in Tables 1-10 follow the format adopted in the third report. All results are normalized with respect to the uniaxial moment capacity [α-0] so that percentage increases can be read off directly. The notation used for percentage steel p*, p or p' follows AASHTO and R.I. stands for the reinforcing index [AASHTO 9.18 - 9.19] given by Eq. 1 and 2 as:

$$\frac{pf_{sy}}{f_c'} + \frac{p^* f^*_{su}}{f_c'} - \frac{p' f_y'}{f_c'} \le 0.3 \qquad \text{for rectangular} \qquad (1)$$

$$\frac{A_s f_{sy}}{b'df_c'} + \frac{A_{sr} f^*_{su}}{b'df_c'} - \frac{A_s' f_y'}{b'df_c'} \leq 0.3 \qquad \text{for flanged} \qquad (2)$$

The terms occurring in Eq. 1 or 2 are defined in Fig. 1.

Parametric studies were conducted to study:

a) Effect of a on fully prestressed members; Table 1 for rectangular sections and Table 7 for flanged sections.

b) b) Effect of a on partially prestressed members without compression steel; Tables 2-4 for rectangular sections and Table 8 for flanged sections.

c) Effect of a on partially prestressed members with compression steel; for rectangular sections in Table 5a, 5b and for flanged sections in Table 6a, 6b.

c) Effect of a on f'c for fully prestressed members; Table 9a for rectangular sections and Table 9b for flanged sections.

2.2 Discussion of Results

As was shown in the third report, the ultimate capacity of a prestressed section is primarily dependent on the amount of steel provided. The introduction of transverse prestressing improves ductility of the concrete and increases its crushing strength, but its influence on the ultimate capacity of the cross-section is somewhat limited.

The following conclusions may be drawn from an inspection of Tables 1-9.

1. The ultimate capacity increases with a and the reinforcing

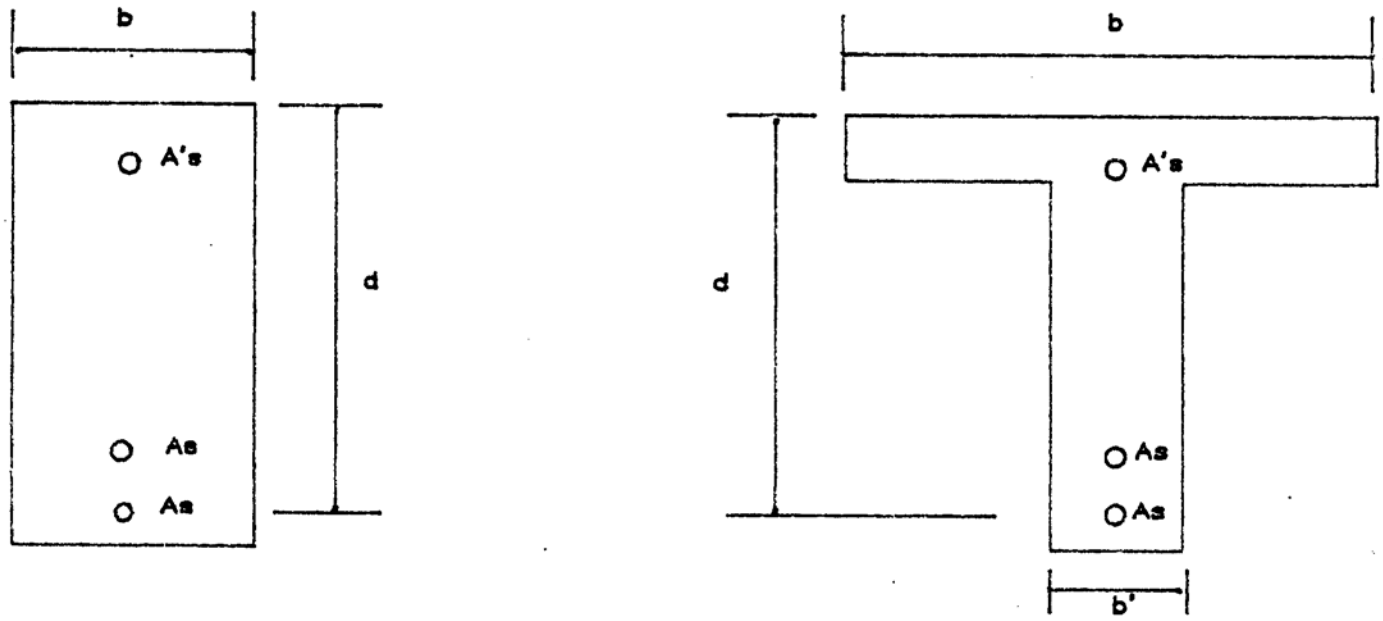

fsy = yield strength of non-pnestressed tension reinforcement

f'y = yield strength of non-prestressed compression reinforcement

As = area of tension steel

Asr = area of steel to develop compression strength of the web of a flanged section

P - As/bd

P - As/bd

P' - A's/bd

Fig. 1 AASHTO details of beams for reinforcing index

Table 1 Effect of α on amount of steel for fully prestressed sections rectangular sections [f'c-5 ksi]

α	R.I. 0.102 p* = 0.002	R.I. 0.193 p* = 0.004	R.I. 0.272 p* - 0.006	R.I. 0.307 p* - 0.007
0.0	1.000	1.000	1.000	1.000
0.05	1.010	1.016	1.037	1.045
0.10	1.019	1.026	1.056	1.072
0.15	1.025	1.033	1.068	1.089
0.20	1.030	1.037	1.076	1.099
0.25	1.033	1.041	1.081	1.106
0.30	1.035	1.043	1.084	1.110
0.35	1.037	1.044	1.086	1.113
0.40	1.038	1.045	1.088	1.114
AASHT0[1]	0.968	0.932	0.916	1 0.913
ACI[1]	0.985	0.964	0.962	1 0.865

Signifies for uniaxial case, i.e. for α = 0

Table la Effect of α on neutral axis position for cases shown in Table 1

α	R.I. 0.102 p* = 0.002 c(0)/c(α)	R.I. 0.193 p* = 0.004 c(0)/c(α)	R.I. 0.272 p* = 0.006 c(0)/c(α)	R.I. 0.307 p* = 0.007 I c(0)/c(α)
0.0	1.000	1.000	1.000	1.000
0.05	0.920	0.923	0.942	0.950
0.10	0.870	0.872	0.895	0.909
0.15	0.836	0.836	0.862	0.878
0.02	0.813	0.812	0.837	0.855
0 .25	0.800	0.795	0.820	0.838
0.30	0.786	0.783	0.808	0.82 7
0.35	0.776	0.774	0.800	0.818
0.40	0.773	0.771	0.795	0.814

Table lb Effect of α on failure stress f^*_{su} for cases shown in Table la

α	R.I. 0.102 p* - 0.002 f*su0/f*suα	R.I. 0.193 p* - 0.004 f*su0/f*suα	R.I. 0.272 p* - 0.006 f*su0/f*suα	R.I. 0.307 p* - 0.007 f*su0,/f*suα
0.0	1.000	1.000	1.000	1.000
0.05	1.007	1.008	1.028	1.037
0.10	1.012	1.012	1.040	1.056
0.15	1.017	1.015	1.045	1.066
0.20	1.020	1.017	1.049	1.071
0.25	1.022	1.018	1.050	1.074
0.30	1.024	1.019	1.051	1.076
0.35	1.025	1.019	1.052	1.077
0.40	1.026	1.020	1.053	1.078

Table 2 Effect of a on amount of steel in partially prestressed rectangular sections [p*-0.002, f'c-5 ksi]

α	R.I. 0.112 P* = 0.002 p = 0.008	R.I. 0.117 p*= 0.002 p = 0.012	R.I. 0.121 p*= 0.002 p = 0.016	R.I. 0.126 p*= 0.002 p = 0.002
0.0	1.000	1.000	1.000	1.000
0.05	1.016	1.018	1.020	1.022
0.10	1.028	1.032	1.035	1.038
0.15	1.038	1.042	1.046	1.050
0.20	1.044	1.050	1.055	1.059
0.25	1.049	1.055	1.060	1.065
0.30	1.052	1.059	1.064	1.069
0.35	1.054	1.061	1.067	1.072
0.40	1.055	1.062	1.068	1.073
AASHT0[1]	0.963	0.961	0.961	0.961
ACI[1]	0.974	0.970	0.968	0.967

Signifies for uniaxial case, i.e. for α = 0

Table 2a Effect of α on neutral axis position for cases shown in Table 2 [p*-0.002]. c(0) and c(a) are the depths of the neutral axis for uniaxial and biaxial cases respectively.

	R.I. 0.112 p = 0.0008 c(0)/c(α)	R.I. 0.117 p = 0.0012 c(0)/c(α)	R.I. .121 p = 0.0016 c(0)/c(α)	R.I. 0.126 p = 0.002 c(0)/c(α)
0.0	1.000	1.000	1.000	1.000
0.05	0.927	0.930	0.930	0.933
0.10	0.878	0.883	0.885	0.887
0.15	0.848	0.854	0.855	0.878
0.20	0.824	0.831	0.832	0.858
0.25	0.809	0.816	0.818	0.836
0.30	0.799	0.805	0.807	0.823
0.35	0.790	0.799	0.802	0.804
0.40	0.787	0.793	0.796	0.801

Table 2b Effect of α on failure stress f* for cases shown in Table 2 [p*=0.002]. f^*_{su0} and $f^*_{su\alpha}$ are the failure stresses for the uniaxial and biaxial cases respectively.

α	R.I. 0.112 p = 0.0008 f*su0/f*suα	R.I. 0.117 p = 0.0012 f*su0/f*suα	R.I. 0.121 P = 0.0016 f*su0 /f*suα	R.I. 0.126 p*= 0.002 f*su0/f*suα
0.0	1.000	1.000	1.000	1.000
0.05	1.006	1.006	1.005	1.005
0.10	1.011	1.010	1.010	1.010
0.15	1.014	1.014	1.013	1.013
0.20	1.018	1.016	1.016	1.015
0.25	1.019	1.019	1.017	1.017
0.30	1.021	1.020	1.019	1.018
0.35	1.022	1.021	1.020	1.019
0.40	1.023	1.021	1.020	1.020

Table 3 Effect of α on amount of steel in partially prestressed rectangular sections [p = 0.004, f'c=5 ksi]

α	R.I. 0.212 p* = 0.004 p = 0.0016	R.I. 0.221 p* = 0.004 p = 0.0024	R.I. 0.228 p* = 0.004 p = 0.0032	R.I. 0.24 p* = 0.004 p = 0.004
0.0	1.000	1.000	1.000	1.000
0.05	1.019	1.020	1.022	1.023
0.10	1.033	1.034	1.036	1.038
0.15	1.042	1.045	1.047	1.049
0.20	1.048	1.052	1.055	1.057
0.25	1.053	1.057	1.060	1.063
0.30	1.056	1.060	1.064	1.067
0.35	1.058	1.062	1.066	1.070
0.40	1.059	1.064	1.068	1.071
AASHT0[1]	0.944	0.948	0.952	0.956
ACI[1]	0.965	0.965	0.966	0.967

Signifies for uniaxial case, i.e. for α - 0

Table 3a Effect of α on neutral axis position for cases shown in Table 3 [p*-0.004]. c(0) and c(a) are the depths of the neutral axis for the uniaxial and biaxial cases respectively.

α	R.I. 0.212 p - 0.0016 c(0)/c(α)	R.I. 0.221 p - 0.0024 c(0)/c(α)	R.I. .228 p - 0.0032 c(0)/c(α)	R.I. 0.240 p - 0.004 c(0)/c(α)
0.0	1.000	1.000	1.000	1.000
0.05	0.925	0.926	0.927	0.928
0.10	0.876	0.877	0.879	0.879
0.15	0.843	0.844	0.845	0.847
0.20	0.819	0.821	0.824	0.824
0.25	0.802	0.805	0.808	0.808
0.30	0.791	0.794	0.796	0.797
0.35	0.783	0.787	0.790	0.790
0.40	0.780	0.784	0.786	0.788

Table 3b Effect of α on failure stress f^*_{su} for cases shown in Table 3 [p*-0.004]. f^*_{su0} and $f^*_{su\alpha}$ are the failure stresses for the uniaxial and biaxial cases respectively.

α	R.I. 0.212 p - 0.0016 f*su0/f*suα	R.I. 0.221 p - 0.0024 f*su0 f*suα	R.I. .228 p - 0.0032 f*su0/f*suα	R.I. 0.241 p* - 0.004 f*su0/f*suα
0.0	1.000	1.000	1.000	1.000
0.05	1.011	1.013	1.015	1.017
0.10	1.016	1.018	1.020	1.024
0.15	1.018	1.021	1.023	1.027
0.20	1.020	1.022	1.025	1.029
0.25	1.021	1.024	1.027	1.030
0.30	1.022	1.024	1.028	1.030
0.35	1.023	1.025	1.028	1.031
0.40	1.023	1.025	1.028	1.032

Table 4 Effect of α on amount of steel in partially prestressed rectangular sections [p*-0.006, f'c - 5ksi]

α	R.I. 0.300 p*- 0.006 f*su0/f*suα	R.I. 0.315 p*- 0.006 f*su0/f*suα	R.I. 0.329 p*- 0.006 f*su0/f*suα	R.I. 0.344 p*- 0.006 f*su0/f*suα
0.0	1.000	1.000	1.000	1.000
0.05	1.041	1.043	1.044	1.045
0.10	1.064	1.068	1.070	1.072
0.15	1.078	1.082	1.086	1.089
0.20	1.087	1.092	1.096	1.108
0.25	1.093	1.098	1.103	1.108
0.30	1.096	1.102	1.108	1.112
0.35	1.099	1.105	1.110	1.115
0.40	1.100	1.106	1.112	1.117
AASHT0[1]	0.863	0.839	0.852	0.797
ACI [1]	0.899	0.875	0.818	0.831

Signifies for uniaxial case, i.e. for α = 0

Table 4a Effect of a on neutral axis position for cases shown in Table 4 [p*-0.006]. c(0) and c(α) are the depths of the neutral axis for the uniaxial and biaxial cases respectively.

α	R.I. 0.300 p - 0.0024 c(0)/c(α)	R.I. 0.315 p - 0.0036 c(0)/c(α)	R.I. 0.329 p - 0.0048 c(0)/c(α)	R.I. 0.344 p - 0.006 c(0)/c(α)
0.0	1.000	1.000	1.000	1.000
0.05	0.945	0.947	0.947	0.948
0.10	0.902	0.904	0.906	0.907
0.15	0.869	0.872	0.875	0.877
0.20	0.844	0.849	0.852	0.854
0.25	0.828	0.832	0.835	0.837
0.30	0.816	0.820	0.824	0.827
0.35	0.808	0.812	0.811	0.819
0.40	0.804	0.808	0.809	0.814

Table 4b Effect of a on failure stress f^*_{su} for cases shown in su Table 4 [p*-0.006]. f^*_{su0} and $f^*_{su\alpha}$ are the failure stresses for the uniaxial and biaxial cases respectively.

α	R.I. 0.300 p - 0.0024 f*su0/f*suα	R.I. 0.315 p - 0.0036 f*su0/f*suα	R.I. .329 p - 0.0048 f*suo/f*suα	R.I. 0.344 p* - 0.006 f*su0/f*suα
0.0	1.000	1.000	1.000	1.000
0.05	1.035	1.038	1.042	1.044
0.10	1.052	1.057	1.063	1.068
0.15	1.060	1.067	1.074	1.081
0.20	1.064	1.072	1.081	1.088
0.25	1.067	1.076	1.084	1.093
0.30	1.069	1.077	1.087	1.095
0.35	1.069	1.079	1.088	1.097
0.40	1.070	1.079	1.089	1.097

Table 5a Effect of α on amount of steel in partially prestressed rectangular sections with compression steel [p*-0.004, p-0.0018, f'c - 5ksi]

	R.I. 0.205 P' = 0.0008	R.I. 0.200 P ' = 0.0012	R.I. 0.195 P ' = 0.0016
0.0	1.000	1.000	1.000
0.05	1.018	1.018	1.017
0.10	1.031	1.030	1.030
0.15	1.040	1.039	1.038
0.20	1.046	1.045	1.044
0.25	1.051	1.050	1.049
0.30	1.054	1.053	1.052
0.35	1.056	1.055	1.054
0.40	1.058	1.056	1.055
AASHT0[1]	0.936	0.932	0.928
ACI[1]	0.966	0.955	0.953

Signifies for uniaxial case, i.e. for α - 0

Table 5b Effect of a on amount of steel in partially prestressed rectangular sections with compression steel [p*-0.004, p-0.0036, f'c - 5ksi]

α	R.I. 0.219 p' = 0.00144		R.I. 0.210 p' = 0.00216		R.I. 0.201 p' = 0.00288
0.0	1.000		1.000		1.000
0.05	1.018		1.018		1.017
0.10	1.033		1.032		1.031
0.15	1.044		1.043		1.042
0.20	1.052		1.052		1.049
0.25	1.057		1.055		1.054
0.30	1.061		1.059		1.058
0.35	1.063		1.062		1.060
0.40	1.065		1 .063		1.062
AASHT0[1]	0.937		0.929		0.921
ACI[1]	0.968		0.968		0.943

Signifies for uniaxial case, i.e. for α = 0

Table 6a Effect of α on amount of steel in partially prestressed rectangular sections with compression steel [p*-0.006, p-0.0024, f'c - 5ksi]

α	R.I. 0.289 p' - 0.00096	R.I. 0.283 p' - 0.00144	R.I. 0.277 p' - 0.00192
0.0	1.000	1.000	1.000
0.05	1.038	1.036	1.035
0.10	1.059	1.056	1.054
0.15	1.072	1.068	1.065
0.20	1.080	1.076	1.073
0.25	1.085	1.081	1.078
0.30	1.088	1.085	1.081
0.35	1.091	1.087	1.084
0.40	1.093	1.089	1.085
AASHT0[1]	0.923	0.916	0.909
ACI[1]	0.884	0.877	0.870

Signifies for uniaxial case, i.e. for α - 0

Table 6b Effect of a on amount of steel in partially prestressed rectangular sections with compression steel [p*-0.006, p-0.0036, f'c - 5ksi]

α	R.I. 0.297 p' = 0.00144	R.I. 0.289 p' = 0.00216	R.I. 0.280 p' = 0.00288
0.0	1.000	1.000	1.000
0.05	1.038	1.036	1.034
0.10	1.060	1.056	1.053
0.15	1.073	1.068	1.064
0.20	1.081	1.076	1.071
0.25	1.086	1.081	1.076
0.30	1.090	1.084	1.079
0.35	1.092	1.087	1.082
0.40	1.094	1.088	1.083
AASHT0[1]	0.924	0.913	0.903
ACI[1]	0.853	0.843	0.834

Signifies for uniaxial case, i.e. for α = 0

Table 6a Effect of α on amount of steel in partially prestressed rectangular sections with compression steel [p*=0.006, p-0.0024, f'c - 5ksi]

α	R.I. 0.289 p' = 0.00096	R.I. 0.283 p' = 0.00144	R.I. 0.277 p' = 0.00192
0.0	1.000	1.000	1.000
0.05	1.038	1.036	1.035
0.10	1.059	1.056	1.054
0.15	1.072	1.068	1.065
0.20	1.080	1.076	1.073
0.25	1.085	1.081	1.078
0.30	1.088	1.085	1.081
0.35	1.091	1.087	1.084
0.40	1.093	1.089	1.085
AASHT0[1]	0.923	0.916	0.909
ACI[1]	0.884	0.877	0.870

Signifies for uniaxial case, i.e. for α - 0

Table 6b Effect of α on amount of steel in partially prestressed rectangular sections with compression steel [p*-0.006, p=0.0036, f'c = 5ksi]

α	R.I. 0.297 p' = 0.00144	R.I. 0.289 p' = 0.00216	R.I. 0.280 p' = 0.00288
0.0	1.000	1.000	1.000
0.05	1.038	1.036	1.034
0.10	1.060	1.056	1.053
0.15	1.073	1.068	1.064
0.20	1.081	1.076	1.071
0.25	1.086	1.081	1.076
0.30	1.090	1.084	1.079
0.35	1.092	1.087	1.082
0.40	1.094	1.088	1.083
AASHT0[1]	0.924	0.913	0.903
ACI[1]	0.853	0.843	0.834

Signifies for uniaxial case, i.e. for α = 0

Table 9a Comparison of effect of a in fully prestressed rectangular sections for f'c - 5 or 7 ksi]

α	p*= 0.004 R.I. 0.193 f'c = 5	p*= 0.004 R.I. 0.142 f' c = 7	p* = 0.006 R.I. 0.272 f' c = 5	p* = 0.006 R.I. 0.205 f' c = 7
0.0	1.000	1.000	1.000	1.000
0.05	1.016	1.012	1.037	1.016
0.10	1.026	1.020	1.056	1.026
0.15	1.033	1.026	1.068	1.033
0.20	1.037	1.031	1.076	1.038
0.25	1.041	1.034	1.081	1.042
0.30	1.043	1.037	1.084	1.044
0.35	1.044	1.038	1.086	1.046
0.40	1.045	1.039	1.088	1.047
AASHTO[1]	0.932	0.949	0.916	0.923
A C I[1]		0.965	0.962	0.946

Signifies for uniaxial case, i.e. for α - 0

Table 9b Comparison of effect of α in fully prestressed flanged sections for f'c - 5 or 7 ksi]

α	p* = 0.002 R.I. 0.154 f' c - 5	p* = 0.002 R.I. 0.074 f' c - 7	p* = 0.0025 R.I. 0.268 f' c - 5	p* = 0.0025 R.I. 0.104 f' c - 7
0.0	1.000	1.000	1.000	1.000
0.05	1.013	1.014	1.024	1.013
0.10	1.022	1.024	1.037	1.023
0.15	1.029	1.032	1.046	1.030
0.20	1.034	1.038	1.052	1.036
0.25	1.038	1.043	1.057	1.040
0.30	1.040	1.045	1.059	1.043
0.35	1.042	1.048	1.061	1.044
0.40	1.043	1.049	1.062	1.045
AASHTO[1]	0.968	0.969	0.964	0.968
ACI[1]	0.983	0.976	0.981	0.977

Signifies for uniaxial case, i.e. for α - 0

index, e.g. Tables 1 or 7.

2. The rate of increase in moment capacity is highest for low α values and levels off after about α - 0.4. The increase is greatest at the highest reinforcing index, e.g. in Table 1 the increase in moment capacity for α = 0.05 is 4.5% for R.I. of 0.307 (marginally over-reinforced] compared to 1% for R.I. of 0.102.

3. The rate of increase in moment capacity is greater for partially reinforced sections with no compression steel than fully prestressed sections, e.g. Table 1 vs Table 2 or Table 7 vs Table 8.

4. The rate of increase in moment capacity declines with increase in f'c, e.g. Table 9.

5. The position of the neutral axis moves up with increasing α. The reduction in this depth can be as much as 25% [see Tables la, 2a, 3a or 4a.

6. The failure stress increases by modest amounts (upto 2%] for R.I. around 0.2. For large R.I. values, increases are much larger, e.g. Table lb, Table 4b.

7. For R.I. of 0.2 (satisfies ACI 18.10.4.3 for re-distribution] increase in ultimate moment capacity ranges from around 1.6% at α = 0.05 to 4.5% for α = 0.4 for fully prestressed members. However, compared to AASHTO formula values, the increases are respectively 9% and 12%

2.3 Analysis of voided section

The ultimate capacity of the voided cross-section shown in Fig. 2 was determined at mid-span and at the support where the section is solid. The results of the analysis are presented in normalized form in Tables l0a and 10b. It may be seen that the increases in the moment capacity match those for a rectangular section shown in Table 1 indicating that the neutral axis falls within the flanges.

2.4 Determination of α

The parametric studies conducted assumed a to be constant over the cross-section. Since both longitudinal and transverse compression stresses vary with depth, it is evident that a is not constant either. It is therefore necessary to estimate average effective longitudinal and transverse stresses from which a single representative a value may be determined.

From a comparison of the biaxial and uniaxial stress strain relations presented earlier [in Fig. 1 of the third report], reproduced as Fig. 3, it may be noted that for strains under 0.0018 there is no difference in the uniaxial and biaxial response. Thus, the a value in this region is of no consequence and may be disregarded. a must be based on the average effective longitudinal and transverse stresses in the more highly stressed zones away from the neutral axis where the strains exceed 0.0018.

The determination of the average effective longitudinal stress poses few problems and a reasonable estimate is given by the Whitney stress.

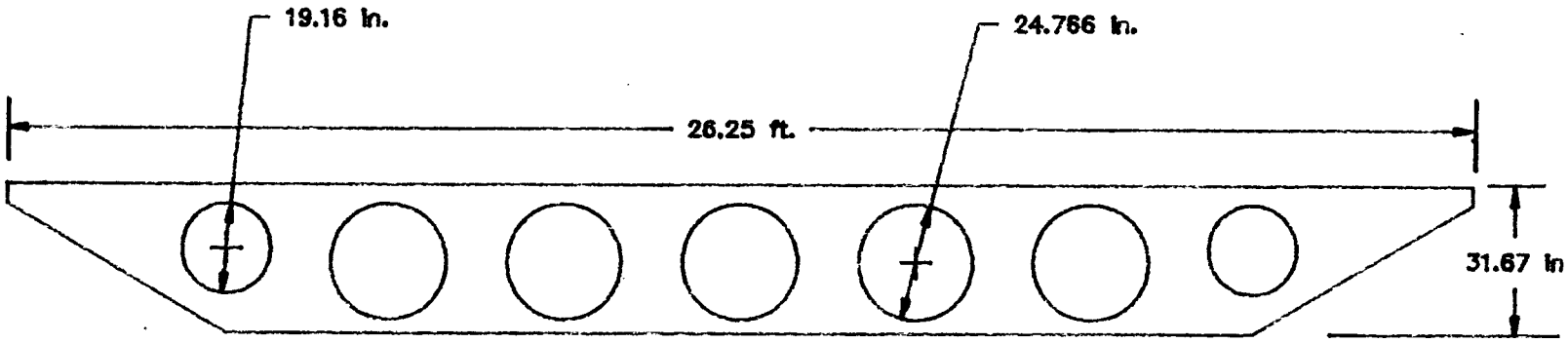

Figure 2. Volded Slob Section

Table l0a Effect of α on amount of steel for fully prestressed solid section at support [f'c-5 ksi]

α	R.I. 0.149 p* = 0.003	R.I. 0.193 p* = 0.004	R.I. 0.234 p* = 0.005	R.I. 0.272 p* = 0.006
0.0	1.000	1.000	1.000	1.000
0.05	1.011	1.015	1.022	1.033
0.10	1.019	1.024	1.035	1.051
0.15	1.025	1.031	1.043	1.062
0.20	1.029	1.035	1.048	1.069
0.25	1.032	1.038	1.052	1.074
0.30	1:034	1.041	1.055	1.077
0.35	1.036	1.042	1.057	1.079
0.40	1.037	1.043	1.057	1.080
AASHT0[1]	0.947	0.928	0.915	0.908
A C I [1]	0.970	1 0.958	1 0.950	1 0.950

Signifies for uniaxial case, i.e. for α - 0

Table 10b Effect of a on amount of steel in fully prestressed voided section [f'c-5 ksi]

α	R.I. 0.149 p*= 0.003	R.I. 0.193 p*= 0.004	R.I. 0.234 p*= 0.005	R.I. 0.272 p*= 0.006
0.0	1.000	1.000	1.000	1.000
0.05	1.011	1.016	1.023	1.033
0.10	1.020	1.025	1.037	1.052
0.15	1.025	1.032	1.046	1.064
0.20	1.030	1.036	1.045	1.072
0.25	1.032	1.040	1.051	1.077
0.30	1.035	1.042	1.057	1.080
0.35	1.036	1.043	1.059	1.083
0.40	1.037	1.044	1.060	1.084
AASHT0[1]	0.950	0.933	0.922	0.912
A C I [1]	0.973	0.962	0.958	0.960

Signifies for uniaxial case, i.e. for α = 0

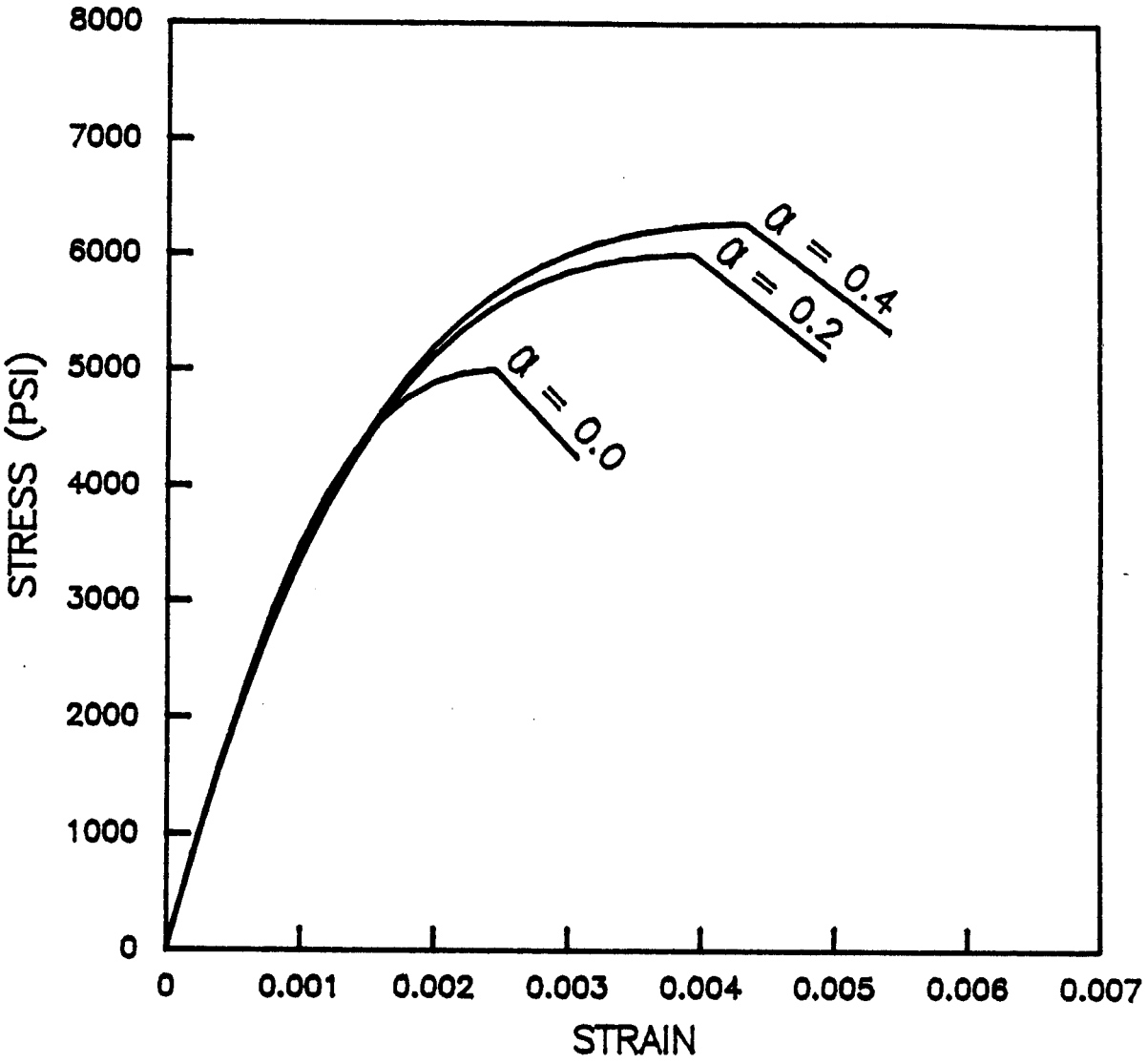

Figure 3. Concrete stress-strain curves for different values of the stress ratio, α

block that assumes it to be .85 f'c. [AASHTO Eq. 9-14]. However, the determination of the effective transverse stress due to prestress in a voided section is more problematic since the cross-sectional area is not constant. Jaeger & Bakht (14) have obtained a closed form solution for the effective area of the voided section by equating the deformation of a solid section of thickness t and unit width to that of a voided one with an opening of depth t_v under the same axial loading. They obtained an expression for the equivalent solid thickness, t_e, of the voided section as:

$$t_e = \left[1 + \lambda a\left(\phi(a) - 1\right)\right]^{-1} \tag{3}$$

where A - t/P_y, P_y = spacing of voids, a m t_v/t and ¢(a) is given as:

$$\phi(a) = \frac{2}{a}\left[\frac{1}{\sqrt{1-a^2}}\tan^{-1}\sqrt{\left[\frac{1+a}{1-a}\right]} - \frac{\pi}{4}\right] \tag{4}$$

The transverse stress in the voided section due to prestress may thus be readily determined from a P/A type analysis using the effective area given by Eq. 3 and 4. The average effective transverse stress in the highly stressed region above the voids may thus be readily determined.

It is of interest to note that the Ontario Highway Bridge Code Commentary [p. 167] stipulates effective transverse prestress limits in the concrete above the voids [i.e. in the highly stressed region that we are interested in] for decks satisfying certain conditions [spans exceeding 1.5 times the deck width but with skews under 25°]. The effective transverse stress due to prestress recommended by OHBDC is 4.5

MPa or 652 psi. For concrete with f'c of 5,000 psi, the average longitudinal stress is 0.85 x 5000 or 4250 psi. Thus, following the guidelines in OHBDC and the concrete strength stipulated by AASHTO, a has a value of 652/4250, around 0.15. The practical range of a values is expected to be less than 0.20.

3. TORSION CAPACITY OF VOIDED SECTIONS

The determination of the torsion capacity of prestressed members was reviewed in the third report. The design procedure recommended is very similar to that for reinforced concrete members and is based on skew bending theory. The torsion strength is contributed partly by the cracked concrete [T'_c] and partly by the reinforcing steel [T_s]. The only unresolved question relates to the evaluation of T'_c [Eq. 8 in the third report] for voided sections. The two approximate approaches mentioned in the last report allow analysis of the voided section as a solid section [$E\eta x^2 y$] with a correction factor F_i to compensate for the reduction in strength due to the openings. These approaches are:

1. Apply the ACI provisions for box sections to the equivalent section, i.e. replace the circular voids by square openings 0.886 times the diameter of the void. The ACI provisions C1 11.6.1.2 stipulate the following correction factor:

$$F_1 - 4h/x \quad \text{for} \quad 0.1x \leq h \leq 0.25x \qquad (5)$$

where h is the overall member thickness and x the shorter dimension. For h exceeding 0.25x, F is unity, i.e. there is no reduction in strength. For h below 0.1x, the design of the cross-section must consider wall stiffness to prevent buckling.

2. Use correction factor proposed by Elliot & Clark (4) on the basis of analytical and experimental studies on voided sections. They proposed:

$$F_2 = 1 - 0.85(t_v/t)^4 \qquad t_v/t \leq 0.81 \qquad (6)$$

where t_v is the diameter of the void and t the overall depth. In the sequel, results of limited comparisons are presented that show the application of Eqs (5) and (6) firstly to a box section and then to a section with circular voids. The results of the application are compared to experimental values presented by Zia & McGee (13).

Example 1 (Fig. 4)

ACI Code Method : x = 9"; h - 2" $.9 \leq 2 \leq 2.25$ OK

$F_1 = 4h/x - 4(2)/9 = .89$

$T_{exp} = 127.2$ in k

$T_{th} = 113.9$ in k

$T_{ex}/T_{th} = \underline{1.12}$

Elliot & Clark (4)

Equivalent dia of void = 5/0.886 = 5.64"

$t_v/t = 0.63 \leq 0.81$ OK

$F_2 = 1 = .85(5.64/9)^4 = .87$

$T_{th} = 111.3$ lb in

$T_{ex}/T_{th} = \underline{1.14}$

Thus for this case, application of both methods lead to very similar results.

Example 2 (Fig. 5)

ACI Code Method: Equivalent square has side 8.5x0.886 = 7.531"

Wall thickness = (12-7.531)/2 = 2.23"

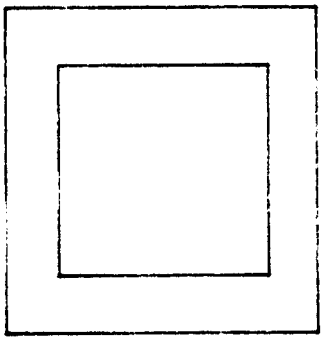

9" x 9" box section

5" x 5" core

x = 9" h = 2"

Figure 4. Example 1 data

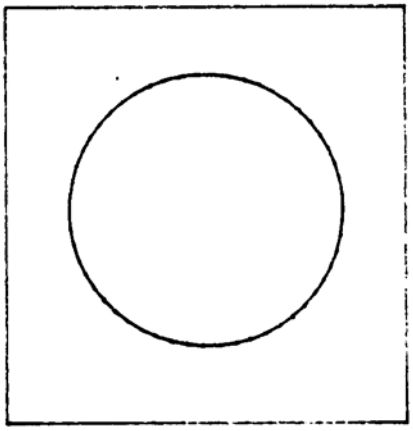

12" x 12" voided section

8.5" diameter core

tv=8.5"

t= 12"

Figure 5. Example 2 data

$1.2 \leq 2.23 \leq 3$ OK

$F_1 = 4h/x = 4(2.23)/12 = 0.748$

$T_{th} = 99.5$ lb in.

$T_{ex} = 120$ lb in; $T_{ex}/T_{th} = \underline{1.21}$

Elliot & Clark (4): t_v - 8.5"; t - 12" tv/t - $0.71 \leq 0.81$ OK

$F_2 = 1-.85(t_v/t)^4 = 1 - .85(8.5/12)^4 = 0.79$

$T_{th} = 104.8$; $T_{ex}/T_{th} = \underline{1.15}$

Thus, in this case, the Elliot & Clark equations are less conservative than the ACI Code equations.

3.1 Recommendations

The results presented show that both Eq. (5) and (6) give acceptable answers. Since Elliot & Clark's (4) factor is easier to use in the case of sections with circular voids, it is proposed that it be used in our study. Thus, to determine T'c in Eq. 8 of the third report, η has to be multiplied by ηF_2.

4. INTERACTION RELATIONS FOR BENDING, TORSION AND SHEAR

The second report reviewed published interaction relations for bending, shear and torsion. In this section, procedures recommended for the determination of the uniaxial bending [M_{uo}]and torsion [T_{uo}]capacities in this study are applied to experimental data to establish new interaction relations.

4.1 Interaction relations for bending and torsion

92 test results for rectangular prestressed sections reported by Bishara (5), Henry & Zia (6) and Mukherjee & Warwaruk (7) were used to evaluate the interaction between bending and torsion. Several researchers, e.g. McMullen and Woodhead (8); Henry & Zia (6) have proposed a circular interaction curve to represent the interaction between moment and shear at failure. The normalized interaction equation for this case is given by:

$$\left[\frac{M_u}{M_{uo}}\right]^2 + \left[\frac{T_u}{T_{uo}}\right]^2 = 1 \qquad (7)$$

where M_u and T_u are the co-existing bending moment and torsion at failure determined experimentally and M_{uo} and T_{uo}, the calculated ultimate flexure and torsion capacities under pure bending or torsion respectively.

The results from 92 tests on rectangular beams are superimposed on a plot of Eq. 7 in Fig. 6. The ultimate flexure capacity of the test

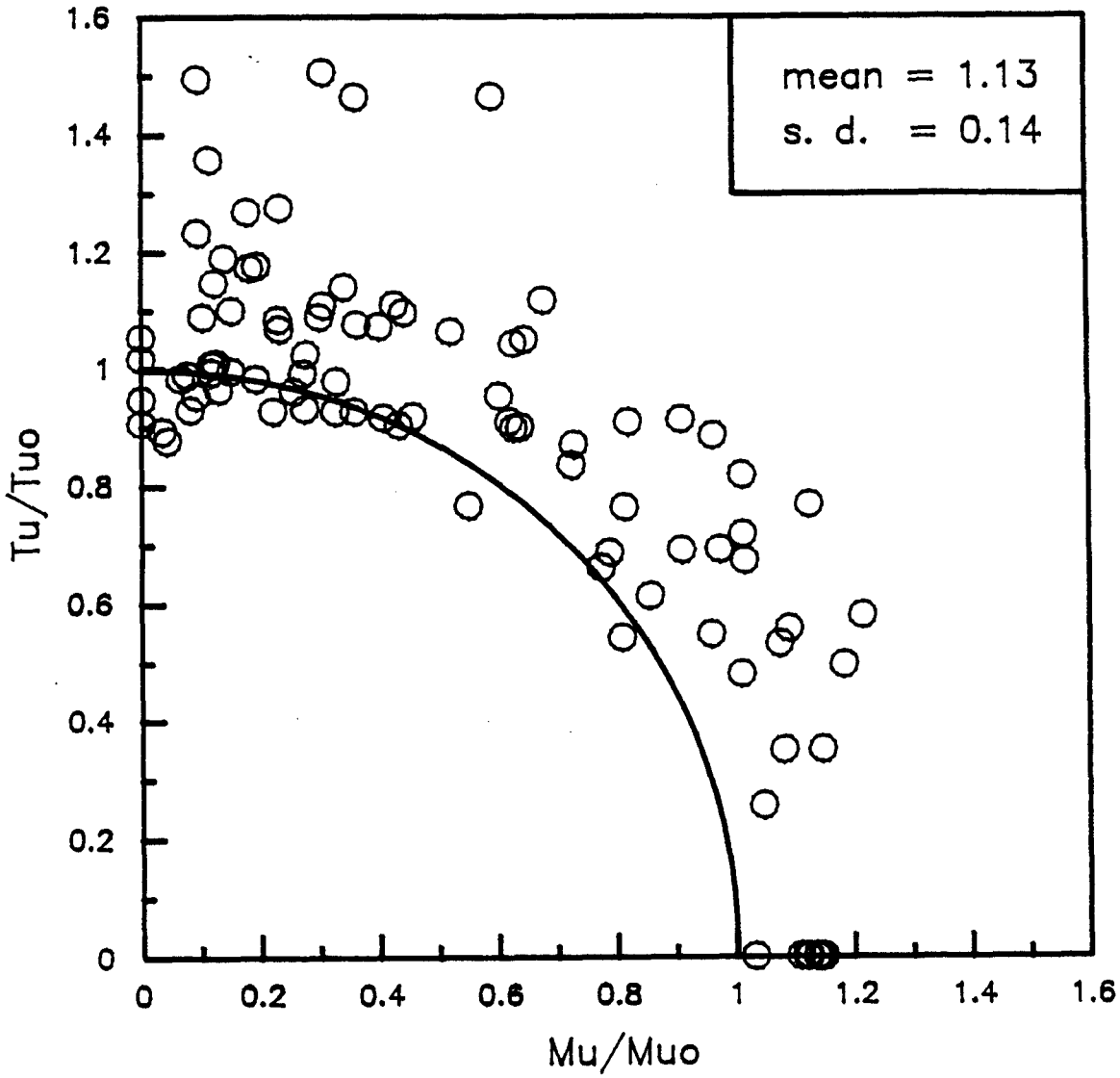

Figure 6. Comparison of 92 test results to the interaction curve for bending and torsion (Eq. 7)

beams, M_{uo}, was determined from program BIAXM (9) using strain compatibility and the ultimate torsion capacity, T_{uo}, from skew bending theory as described in the third report. In each case, the capacity reduction factors were assumed to be unity so that an accurate assessment of the true factor of safety implied by the interaction relations could be made.

The mean value of the factor of safety was found to be 1.13 with a standard deviation of 0.14. Of the 92 test beams, Eq. 7 failed to predict failure for 18 beams or 19.6% of the sample examined. However, as the mean and standard deviation values indicate, the correlation between experiment and theory is generally quite good.

From the design standpoint, the principal drawback of Eq. 7 is the need to check for interaction even when the relative proportions of moment $[M_u/M_{uo}]$ or torque $[T_u/T_{uo}]$ are small. In order to circumvent this problem, new interaction relations were investigated that attempted to reduce the number of checks.

The first interaction'relation examined is shown in Fig. 7. It may be seen that the circular interaction curve in Fig. 6 has been replaced by three straight lines. Although the use of three lines may be less elegant mathematically, from the designer's viewpoint this offers the advantage that the number of checks is substantially reduced.

Thus, for the interaction relation shown in Fig. 7, no checks are needed if:

$$M_u/M_{uo} \leq 0.5 \tag{8}$$

or $$T_u/T_{uo} \leq 0.2 \tag{9}$$

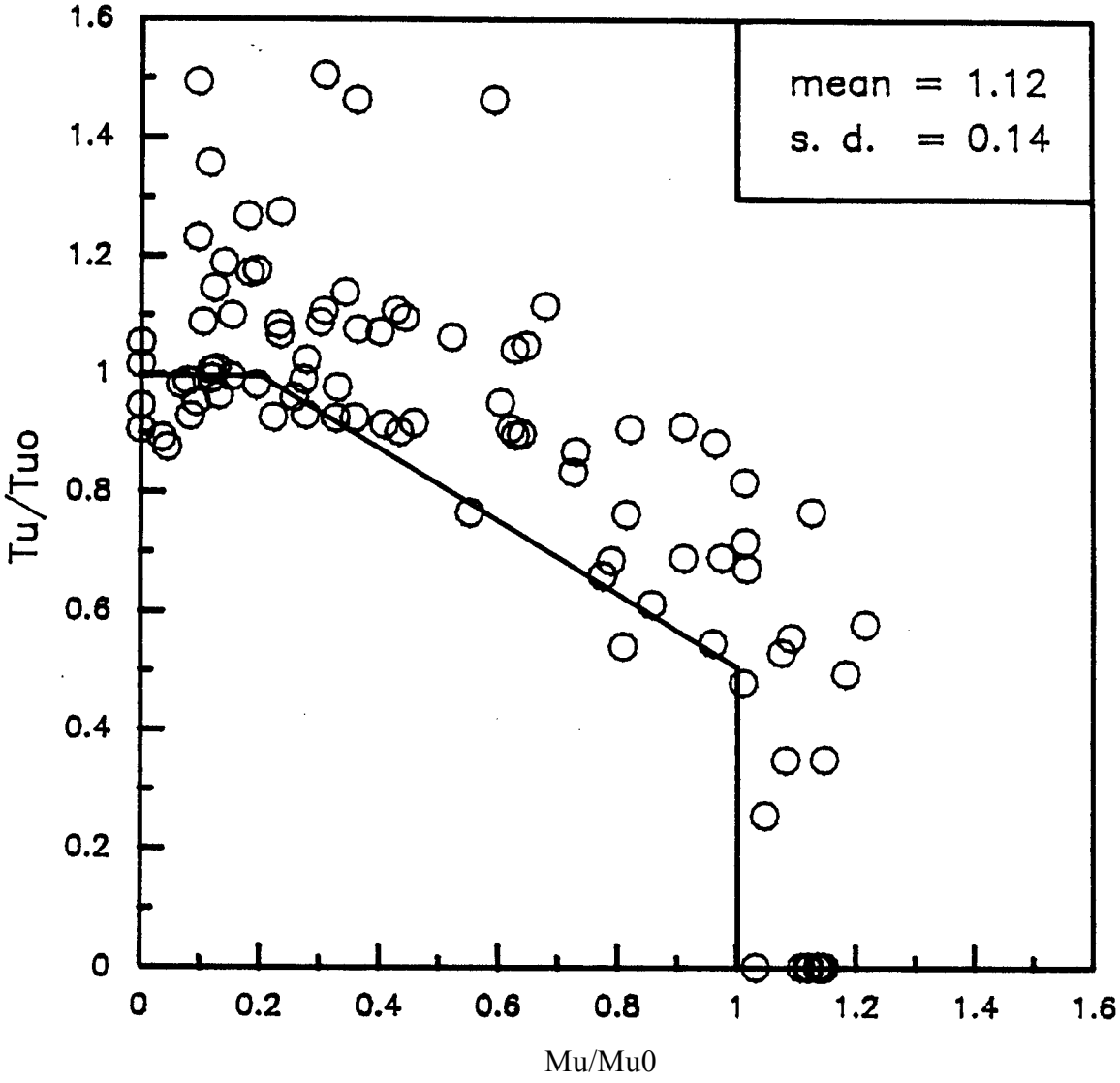

Figure 7. Comparison of 92 test results to the interaction curve for bending and torsion (Eqs. 8, 9, and 10)

If conditions (8) or (9) are not met then condition (10) needs to be satisfied;

$$\frac{5M_u}{9M_{uo}} + \frac{8T_u}{9T_{uo}} \leq 1 \qquad (10)$$

Application of conditions 8-10 to the 92 test results indicates the correlation between theory and experiment is somewhat improved with the average factor of safety reducing to 1.12 from 1.13 and the standard deviation remaining unchanged at 0.14. The number of test cases where failure was not anticipated also dropped by one to 17 or 18.5% of the sample compared to 19.6% given by Eq. 7.

In order to determine whether condition (9) could be further extended, another set of interaction relations, shown in Fig. 8 were examined. In this case the limit on condition (9) was set as 0.3, i.e.

$$\text{or} \qquad T_u/T_{uo} \leq 0.3 \qquad (11)$$

but condition (8) remained unchanged. As a consequence, the equation of the sloping line is altered to:

$$\frac{10M_u}{17M_{uo}} + \frac{14T_u}{17T_{uo}} \leq 1 \qquad (12)$$

Inspection of Fig. 8 indicates that the application of conditions (9), (11) and (12) improves the correlation between experiment and theory [the average factor of safety reduces from 1.13 to 1.11, compared to Eq. 7 with the standard deviation remaining unchanged at 0.14] but the number of specimens where failure was not predicted increased from 18 to 24 or 26.1% of the sample size.

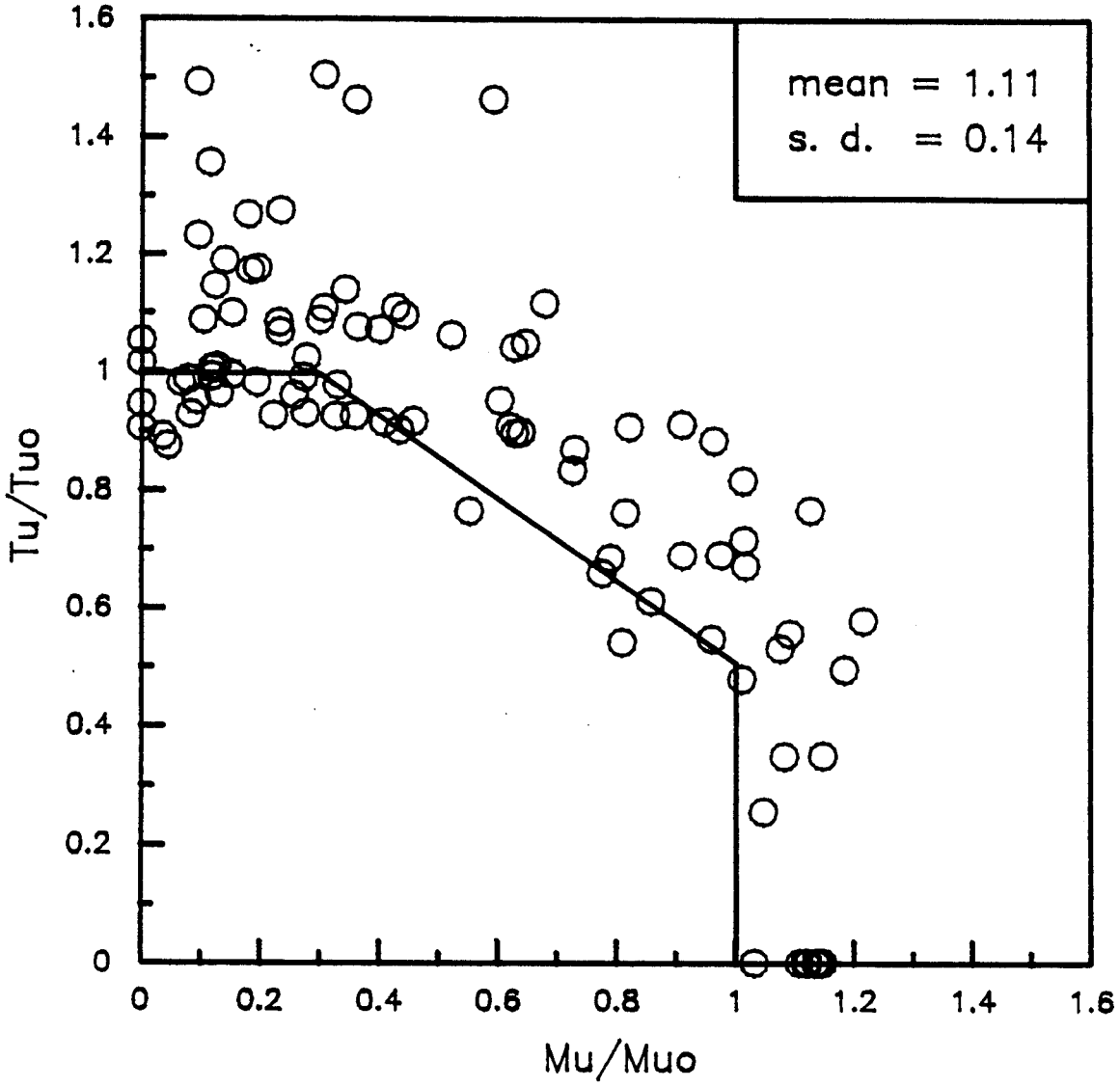

Figure 8. Comparison of 92 test results to the interaction curves for bending and torsion (Eqs. 8, 11, and 12)

Results of the 3 interaction factors examined are summarized in Table 11. It appears that the proposed relations given by Eqs. 8-10 (Fig. 7) are the most appropriate and will be adopted in this study.

4.2 Interaction relations for torsion and shear

40 test results from Bishara (5) and Henry & Zia (6) were used to evaluate the interaction relations for torsion and shear available in the published literature.

Several investigators, e.g. Mukherjee & Warwaruk (7); Henry & Zia (6) have proposed straight line interaction relations that combine the simultaneous effect of shear and torsion. The normalized equation for this case is given by Eq. 13 as:

$$\frac{T_u}{T_{uo}} + \frac{V_u}{V_{uo}} = 1 \qquad (13)$$

where T_u and V_u are the co-existing torsion and shear at failure and T_{uo} and V_{uo} the calculated ultimate capacities under pure torsion or the shear respectively.

The results of 40 tests on rectangular beams are superimposed on a plot of Eq. 13 in Fig. 9. The ultimate shear capacity of the test beams, V_{uo}, was determined in accordance with the AASHTO provisions and the torsion capacity, T_{uo}, from skew bending theory. As before, the capacity reduction factors were assumed to be unity so that an accurate assessment of the true factor of safety implied by the interaction relations could be made.

Table 11 Comparison of interaction relations for bending and torsion

Description	Interaction relations for bending & torsion (1)	(2)	(3)
Definition	I Eq. 7	Eq. 8-10	Eq. 8, 11-12
Plot	Fig. 6	Fig. 7	Fig. 8
Mean	1.13	1.12	1.11
Standard Deviation	0.14	0.14	0.14
# wrongly predicted	18 out of 92 (19.6%)	17 out of 92 (18.5%)	26 out of 92 (26,10
Checks Needed	Always	Only if Eqs. 8 or 9 is not satisfied	Only if Eq. 8 or 11 is not satisfied

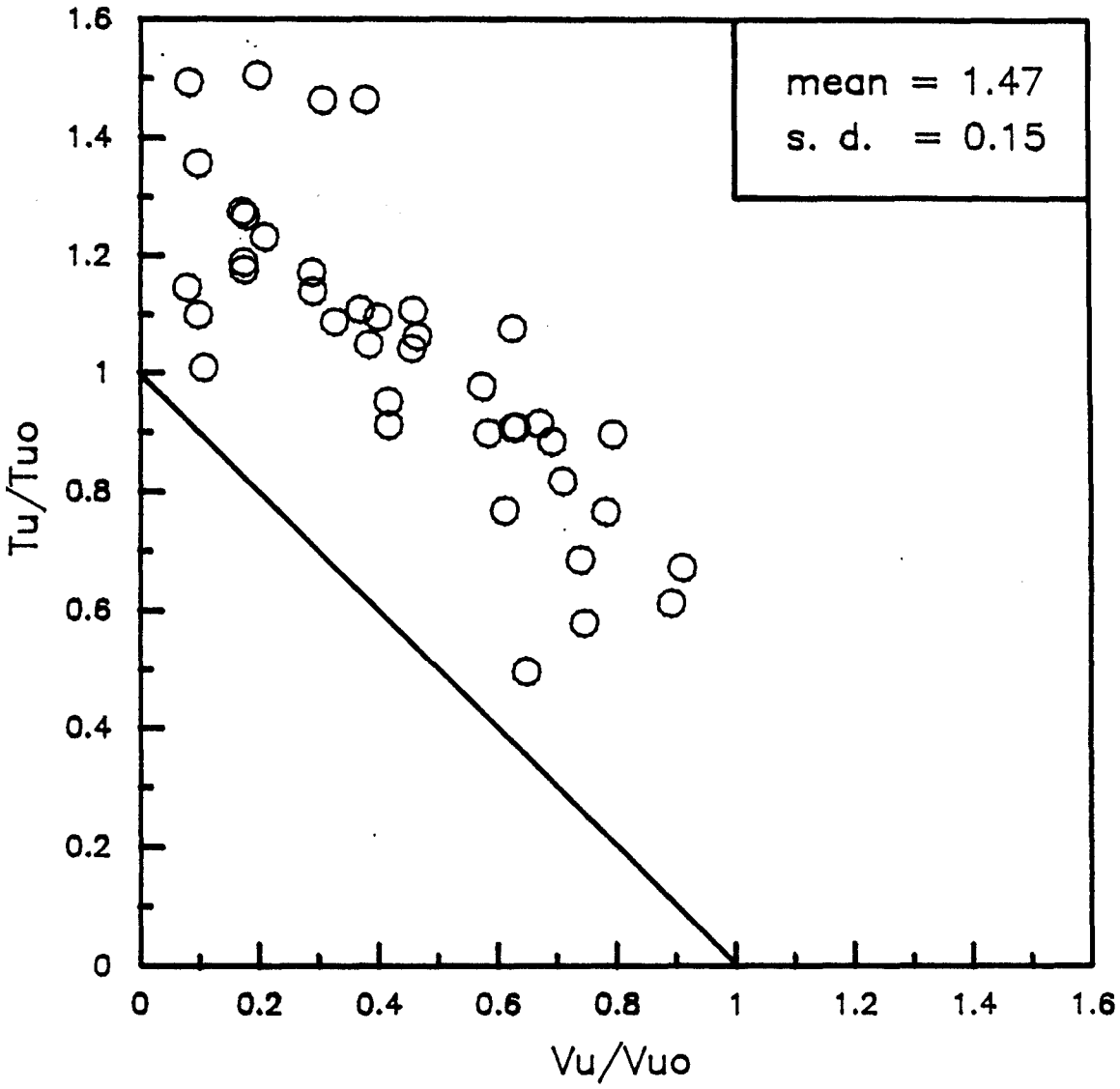

Figure 9. Comparison of 40 test results to the interaction curve for shear and torsion (Eq. 13)

The mean value of the factor of safety was found to be 1.47 with a standard deviation of 0.15. As is evident from Fig. 9, all the beams failed as predicted so that all test results fall outside the region bounded by the Eq. 13 and the coordinate axes.

It was mentioned earlier, that the main drawback of simple interaction equations such as Eq. 13, is their requirement for checks irrespective of the magnitudes of torsion and shear acting on the beam. In order to correct this situation, a new interaction relation, identical to that considered for interaction between bending and torsion was investigated. This required no checks when conditions 14 or 15 were satisfied but condition 16 to be complied otherwise:

$$V_u/V_{uo} \leq 0.5 \tag{14}$$

$$T_u/T_{uo} \leq 0.2 \tag{15}$$

$$\frac{5V_u}{9V_{uo}} + \frac{8T_u}{9T_{uo}} \leq 1 \tag{16}$$

Fig. 10 shows the application of Eqs. 14-16 to the test data. The average factor of safety reduces from 1.47 to 1.18 compared to the application of Eq. 13, with the standard deviation also reducing to 0.14 from 0.15. However, conditions 14-16 were unable to predict failure for two beams [5% of sample examined].

If the limit on condition 15 is increased to 0.3 [as in the case investigated for the effects of bending and torsion, Fig. 8], conditions 15 and 16 are modified as:

$$T_u/T_{uo} \leq 0.3 \tag{17}$$

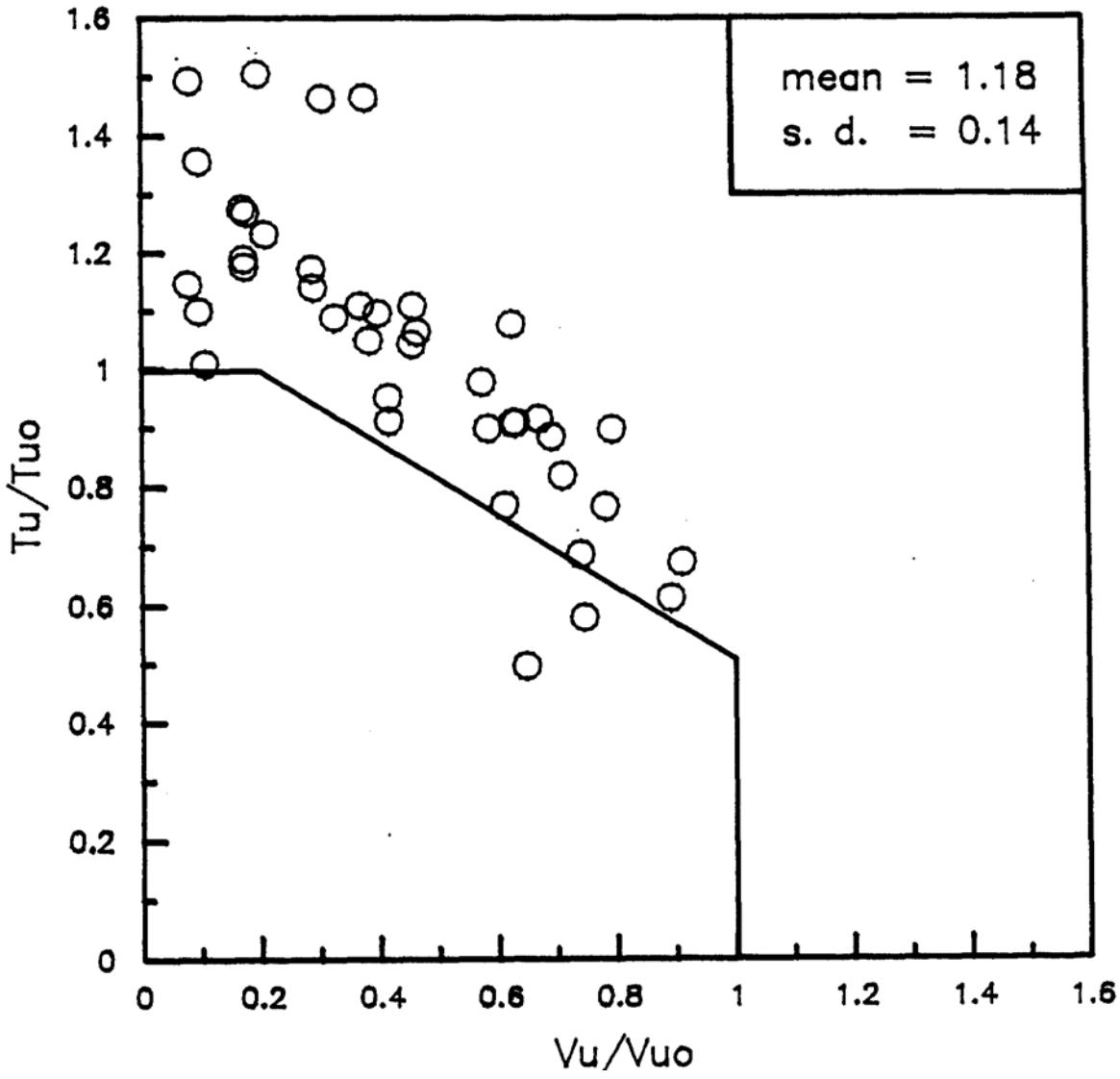

Figure 10. Comparison of 40 test results to the interaction curve for shear and torsion (Eqs. 14, 15, and 16)

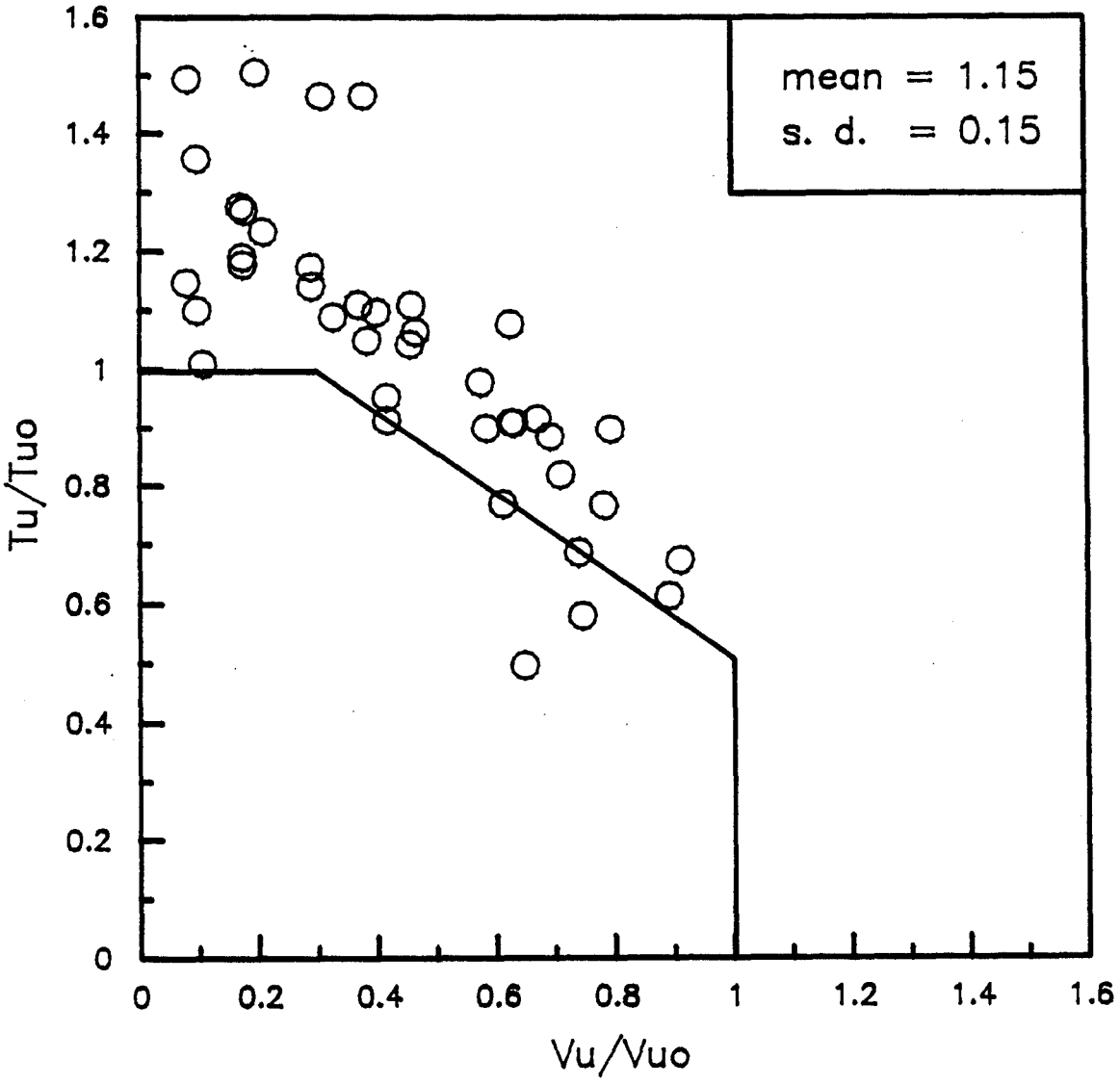

Figure 11. Comparison of 10 test results to the interaction curve for shear and torsion (Zqs. 14, 17, and 18)

$$\frac{10V_u}{17V_{uo}} + \frac{14T_u}{17T_{uo}} \leq 1 \qquad (18)$$

Application of conditions 14, 17 and 18 is shown in Fig. 11. This shows that the factor of safety reduces from 1.47 [Eq. 13] to 1.15 with the standard deviation remaining unchanged at 0.15. However, the number of failures not anticipated increased to five or 12.5% of the sample size.

Table 12 summarizes the results of the application of the three interaction relations. From the comparisons presented in this table, the application of conditions 14-16 appears to give the most satisfactory results. It should be noted that the form of these interaction relations is identical to that for bending and torsion [Eq. 8-10], making it rather attractive from the standpoint of design.

4.3 Application to curved prestressed girders

The interaction relations examined were based on tests on straight prestressed beams. In order to test their validity in applications involving curved postensioned girders, interaction relations considered are applied to such girders.

The only test results available are those reported by Lee (10). Three girders were considered and failure occurred in two cases due to combined bending and torsion and in one case due to shear and torsion. The results of Lee's tests are superimposed on the interaction relations proposed shown in Figs. 12 and 13. It may be seen that whereas the interaction relations for bending and torsion correctly predict the.

Table 12 Comparison of interaction relations for shear and torsion

Description	Interaction relations for shear & torsion (1)	(2)	(3)
Definition	Eq. 13	Eq. 14-16	Eq. 14, 17-18
Plot	Fig. 9	Fig. 10	Fig. 11
Mean	1.47	1.18	1.15
Standard Deviation	0.15	0.14	0.15
# wrongly predicted	None	2 out of 40 (5%)	5 out of 40 (12.5%)
Checks Needed	Always	Only if Eq. 14 or 15 is not satisfied	Only if Eq. 14 or 15 is not satisfied

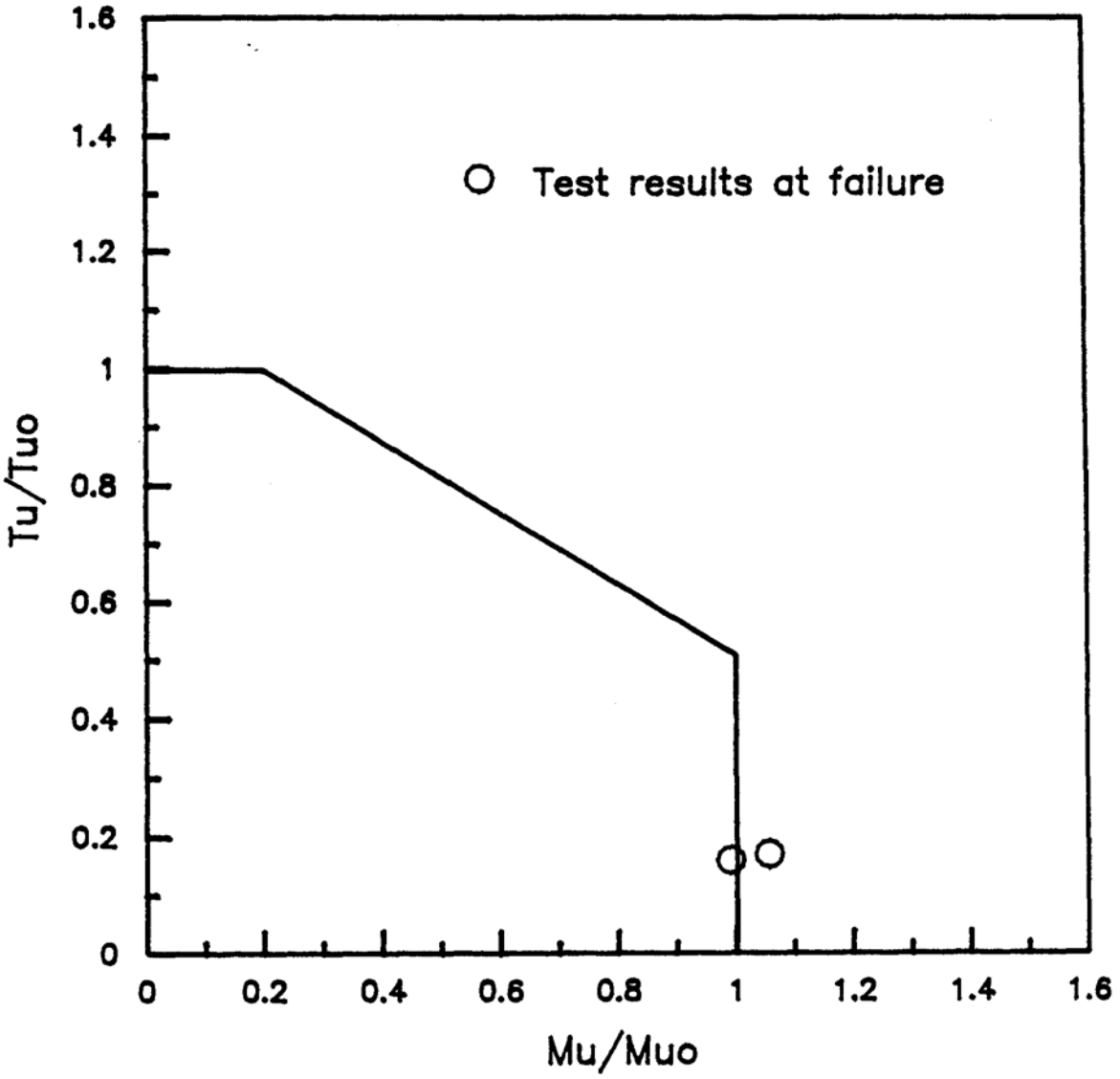

Figure 12. Comparison of 2 test results for curved beams by Lee (10) with the interaction curve for bending and torsion (Eqs. 9 and 10)

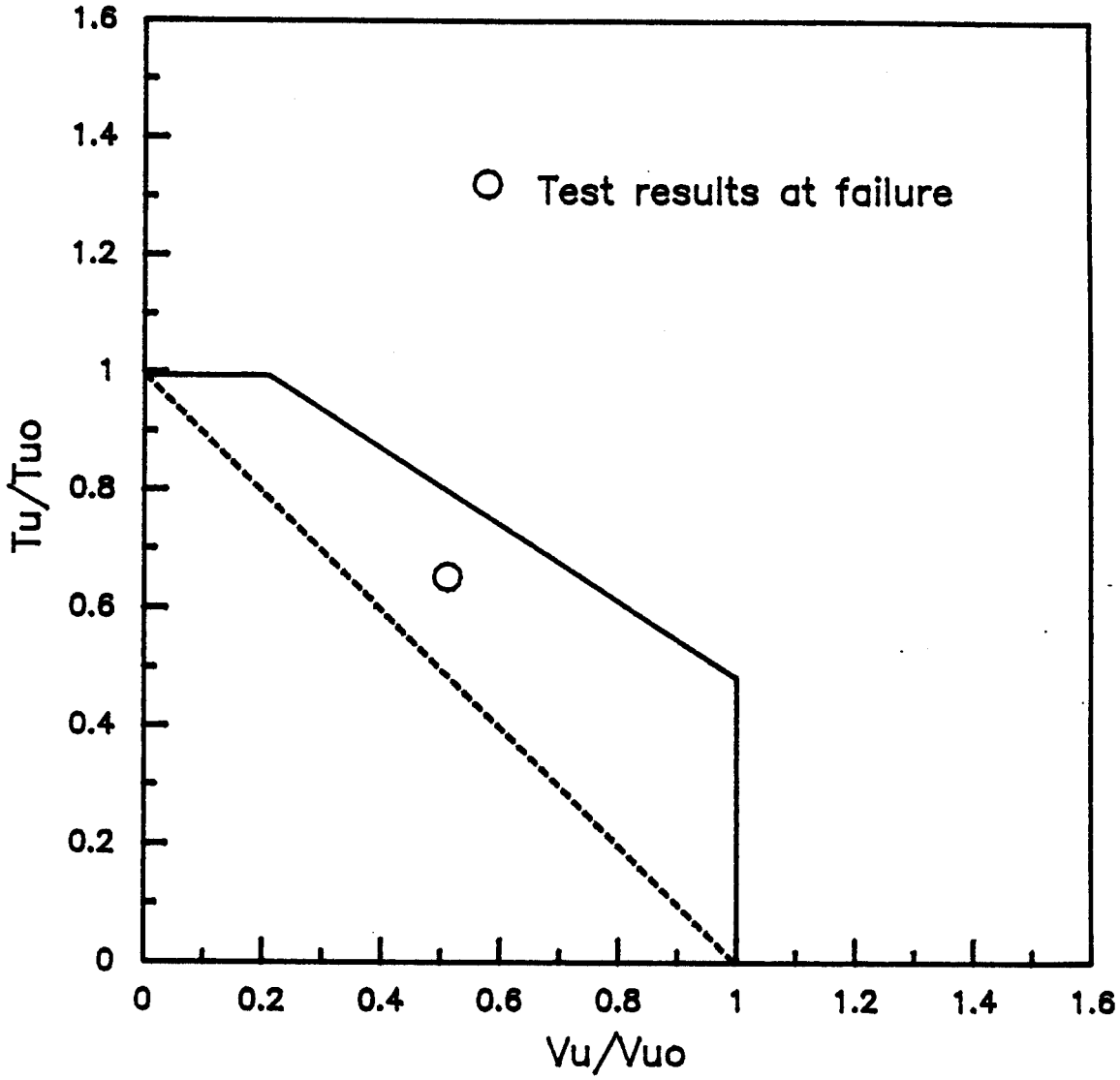

Figure 13. Comparison of 1 test result for curved beams by Lee (10) with the interaction curves for shear and torsion (Eq. 13 and Eqs. 14, 15, and 16)

failure in Fig. 12, such is not the case for shear and torsion in Fig. 13. For this case, Zia's interaction relations give better results. However, there is some uncertainty regarding the interpretation of Lee's test data and further investigations are in progress.

4.4 Recommendations

On the basis of the investigations made, the following recommendations are made:

1. Bending & Torsion - Eqns 8-10

2. Torsion & Shear - Eqns 14-16 - straight girders

- Eqn 13 - curved girders (under investigation)

It is worth noting that AASHTO uses similar interaction relations, e.g. effect of bending and shear for designing web panels of plate girders [Eq. 10-109, C1. 10.48.5.4].

5. DETERMINATION OF COLLAPSE LOAD

The determination of the theoretical collapse load will be discussed in the next phase of the study in which models will be tested to failure. For completeness, a brief description on re-distribution is included in Section 5.2 followed by an outline of a procedure that may be adopted to estimate the theoretical failure load in Section 5.3.

5.1 Background

The procedures outlined in Chapters 2-4 allow the determination of the ultimate resistance at a section. A conservative estimate of the ultimate strength of the structure may be obtained by assuming failure to occur when the interaction relations fail at any section. The true ultimate load, however will be somewhat greater in most cases due to redistribution of forces.

The distribution of forces in an indeterminate structure depends on the relative stiffnesses of its members. As sections crack and stiffnesses are reduced, the pattern of forces change from that derived from linear elastic analysis. Provided adequate ductility is assured, a section that can sustain no further load may be regarded as a plastic hinge where rotation can freely take place. The ultimate load capacity of the structure is reached when the formation of successive hinges at critical sections transforms it into a mechanism. Ideally a structure that is statically indeterminate to the nth degree, fails after n plastic hinges have formed and the remaining plastic hinge or hinges are

just about to develop. This provides an upper bound on the strength of the structure and is referred to as full redistribution of forces.

As noted above, the extent of redistribution possible in a structure is limited by its ductility. For prestressed structures, this is governed by the amount of steel provided. Even so, the ductility of concrete structures is small compared to steel structures and full redistribes not permit re-distribution, the ACI Code [C1.
18.10.4] allows upto 20% of the negative moments to be redistributed provided the maximum steel limits are satisfied [C1 18.10.4.3].

5.2 Procedure for calculation of collapse load

The procedure to be examined for estimating the collapse load of the curved, continuous, prestressed structure is a modification of that described by Cohn & Frostig (11) for determining the ultimate flexure strength of indeterminate straight beams. In essence, it is a stepwise elastic analysis to collapse in which the behavior of the structure is assumed to be linear between the formation of plastic hinges. The assumptions implicit in the analysis are as follows:

1. Bond between pretensioned steel and concrete is assured.

2. Moment-curvature and torque-twist relations for the prestressed section justify the validity of the conventional plastic hinge concept.

3. Shear failure is prevented by appropriate lateral reinforcement.

4. Member stiffness is based on gross concrete sections.

5.3 Steps in analysis

1. Idealize prestressed structure as a beam and determine elastic properties based on the gross concrete section. Degree of indeterminacy is n.
2. Separate loading into three categories:
   a) dead load b) unit live load and c) effective prestress.
3. Complete elastic analysis for above loadings.
4. Determine lowest value of live load w_i at which combination of internal forces results in the formation of a plastic hinge, i.e. interaction relation fails at a critical section. No factors are used on dead load or prestress effects.
5. Replace location of plastic hinge by actual hinge and repeat steps 3 and 4 n times until mechanism forms. Note that when structure becomes determinate due to formation of plastic hinges, secondary moments due to prestress will automatically disappear.
6. Collapse load is given by Zw_i.

The major assumption is that sections possess adequate ductility so that full re-distribution is permitted. Modifications may be needed to assess whether this is the case by examining the moment-curvature and torque twist relations at the sections where hinges are assumed to form. For this case, failure may result prior to mechanism formation, i.e. there is limited re-distribution. The preliminary results of this study are expected to be included in Hodge's (12) forthcoming thesis.

6. FINITE ELEMENT MODELING

During the last quarter of this research effort finite element computer modeling of a two span curved slab structure was completed. As mentioned in the third quarterly report on May 8, 1987 word was received from the Florida Department of Transportation that they would like a cross section which possessed 33% voids, so that it more closely matched the typical Ontario, Canada design which had approximately 34% voids. This new modeling was completed during this last quarter. This section of the report will discuss the slab modeling; results of longitudinal posttensioning loading, transverse posttensioning loading, and gravity loading; and discussion of these results.

6.1 Finite Element Model Development

The Florida Department of Transportation expressed the desire to have the width of the slab 26.25 feet (one 12 foot lane, two 6 foot shoulders, and two 15 inch parapets). They also wanted the cross section to have 33% voids. Also, as discussed in the second quarterly report, they wanted a model that showed a definite radius of curvature and one which, with a 1 to 3.5 test model, would fit into a testing laboratory. For this latter purpose, as discussed in the second quarter report, two spans each of 50 feet with a radius of curvature of the centerline of the slab of 127.3 feet which encompassed an angle of 45^0 was

chosen. In order to accomplish the 33% void cross section, several typical Canadian curved span parameters were used. These are listed below.

1. Large void diameter to slab depth = .782
2. Small void diameter to slab depth = 0.605
3. Spacing between larger voids = 0.12 of slab width
4. Spacing between larger and smaller voids = 0.11 of slab width
5. Flange length = 0.15 of slab width
6. Flange depth = 0.38 of slab depth

It was arbitrarily chosen to use five central circular voids and two, one at each edge of the slab, smaller voids. Using all of these parameters an equation was established for the void content of the slab (which was set at 0.33 of the overall content) in terms of the depth of the slab. This depth was then found to be 31.67 inches. Therefore the following dimensions were established.

1. Large void diameter = 0.782 (31.67) = 24.766 inches
2. Small void diameter = 0.605 (31.67) = 19.16 inches
3. Spacing between larger voids = 0.12 (26.25)(12) = 37.8 inches
4. Spacing between larger and smaller voids = 0.11 (26.25)(12) = 34.65 inches
5. Flange length = 0.15 (26.25)(12) = 47.25 inches
6. Flange depth = 0.38 (31.67) = 12.03 inches

Therefore, as one will observe, the total rectangular area discounting the flanges and voids was

$$(26.25)(12)(31.67)= 9976.05 \text{ in.}^2$$

The flange area removed was

$$(2)(1/2)(47.25)(0.62)(31.67) = 927.77 \text{ in.}^2$$

The area of the five larger central voids and the two outside smaller voids was

$$(5\pi/4)(24.766)^2 + (2\pi/4)(19.16)^2 = 2985.29 \text{ in}^2$$

thus the void ratio for this cross section was found to be void ratio = 2985.29/9048.28 = 0.33 as required. A picture of this determined cross section is shown in Figure 11. This is the cross section that was used during the last quarter finite element analyses of the two span, curved, voided slab.

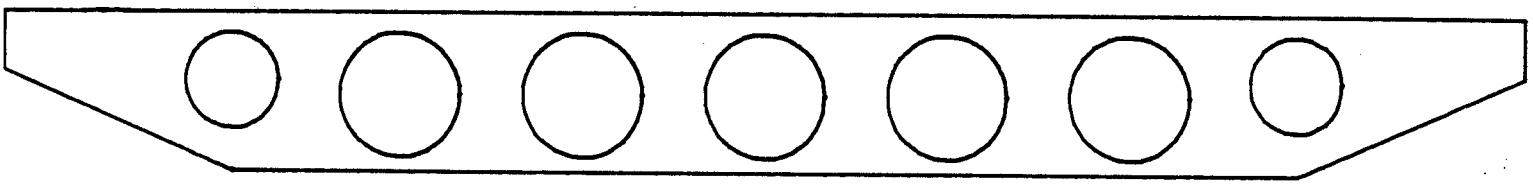

Figure 14. Final Cross Section with 33% Voids.

Two meshed finite element models were developed, where one model had a finer longitudinal and transverse mesh size, so that the variation of the results could be ascertained with respect to the mesh size. Due to geometric longitudinal symmetry (i.e. two simply supported spans) and loading symmetry (i.e. same load on each span), only one span, encompassing 22.5^0 with simple supports on either end and other appropriate symmetry boundary conditions, had to be analyzed. From a typical Canadian design the ratio of the top cover over the voids to the bottom cover was found to be 1.385. Using this same ratio for these models it was calculated that the top cover was 4.009 inches, while the bottom cover was 2.895 inches. Figure 12 shows the resulting meshed finite element model of the voided cross section for the coarser meshed model, NCURM.Figure 13 shows the corresponding meshed cross section for the finer meshed model, NFCURM. The typical Canadian design had solid sections near each simple support.

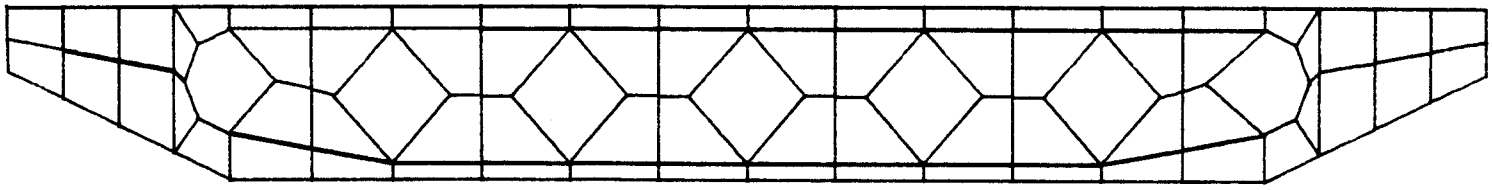

FIGURE 15. Meshed Voided Cross Section for the Coarser Meshed Model, NCURM

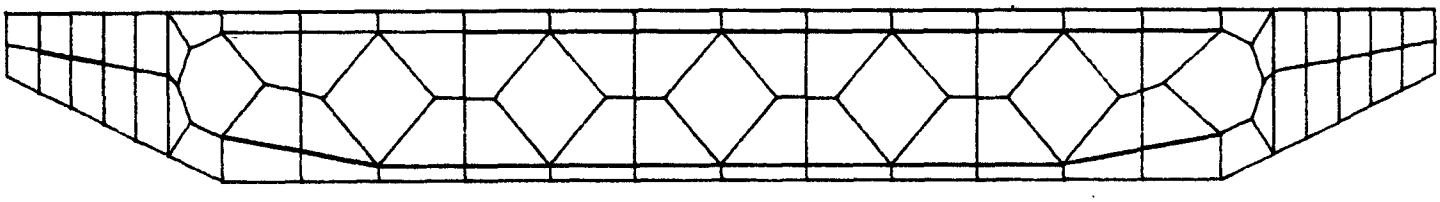

FIGURE 16 . Meshed Voided Cross Section for the Finer Meshed Model, NFCURM

The length of the solid section near an end support for the typical Canadian design was 0.0695 of the span length. This same ratio yielded a length of 1.564^0 for these finite element models. Simple supports were thus established at one end of the slab at each node along the bottom of the cross section. The length of the solid section near the center support of the two spans for the typical Canadian design was 0.20725 of the span length. Using this same ratio the length of the solid section at the center support for these finite element models was found to be 2.33^0. This simple support at the center of the two spans was modeled by specifying a simple support at the bottom center node of the cross section. For longitudinal symmetry reasons, rotation about a radial line of the nodes at the center of span was restricted. Figure 14 shows the overall structural shape of the coarser meshed finite element model, NCURM. Figure 15 shows the overall structural shape of the finer meshed finite element model, NFCURM.

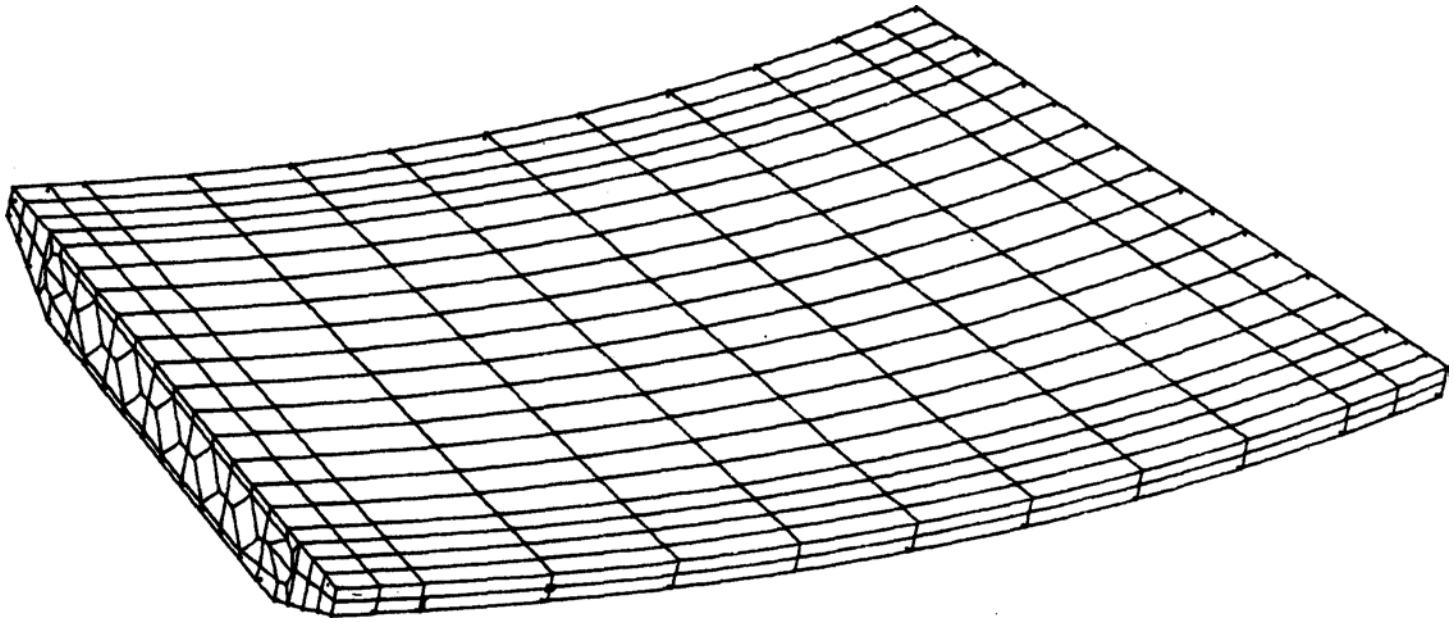

FIGURE 1-7. Overall Structural Shape of Coarser Meshed Finite Element Model, NCURM.

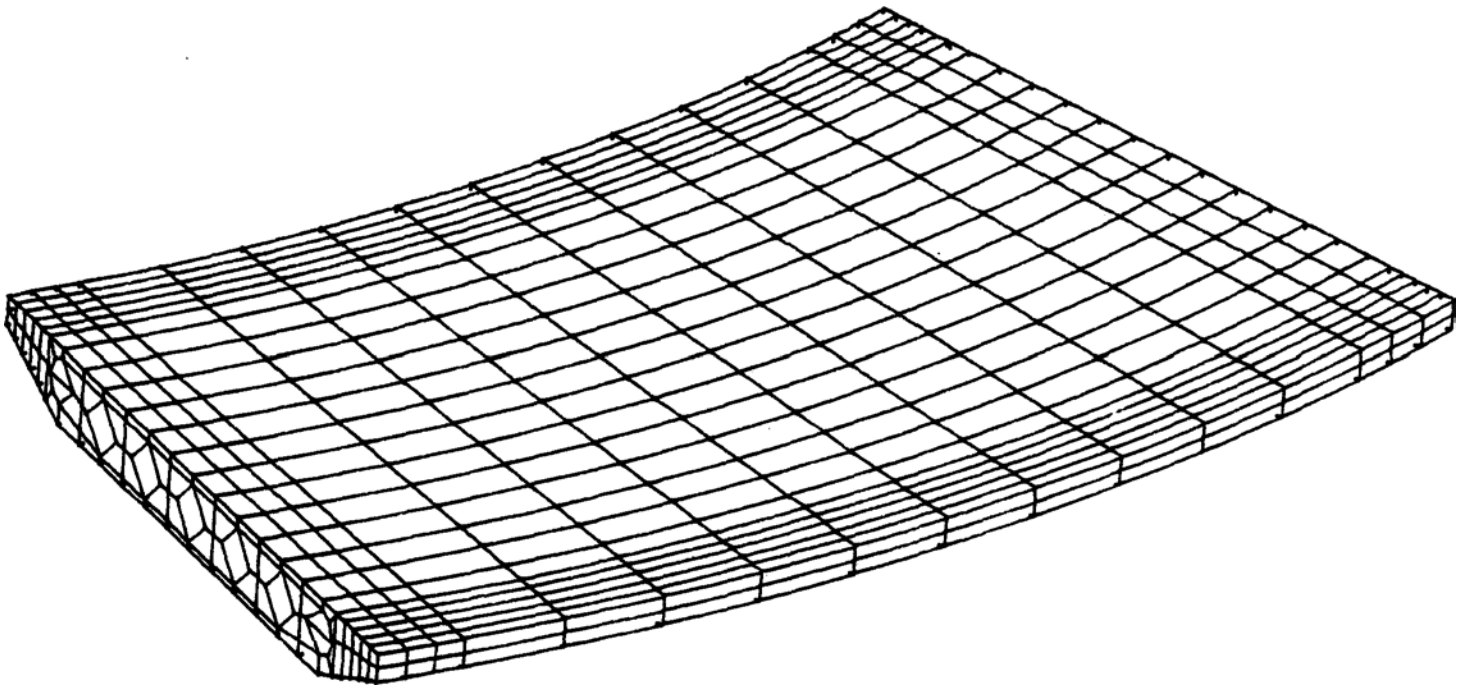

FIGURE 18. Overall Structural Shape of Finer Meshed Finite Element Model, NFCURM.

As was previously done with other models, described in the previous quarterly reports, once the six-sided, eight noded solid element models were formed, thin plate elements (0.01 inches thick) were attached to the top and bottom of these structural models. These thin plate elements would enable an easier determination of stress variations on the top and bottom surfaces of the slab, when the slab was loaded. Figure 16 shows a typical view of these thin plate elements for the coarser meshed finite element structural model, NCURM.

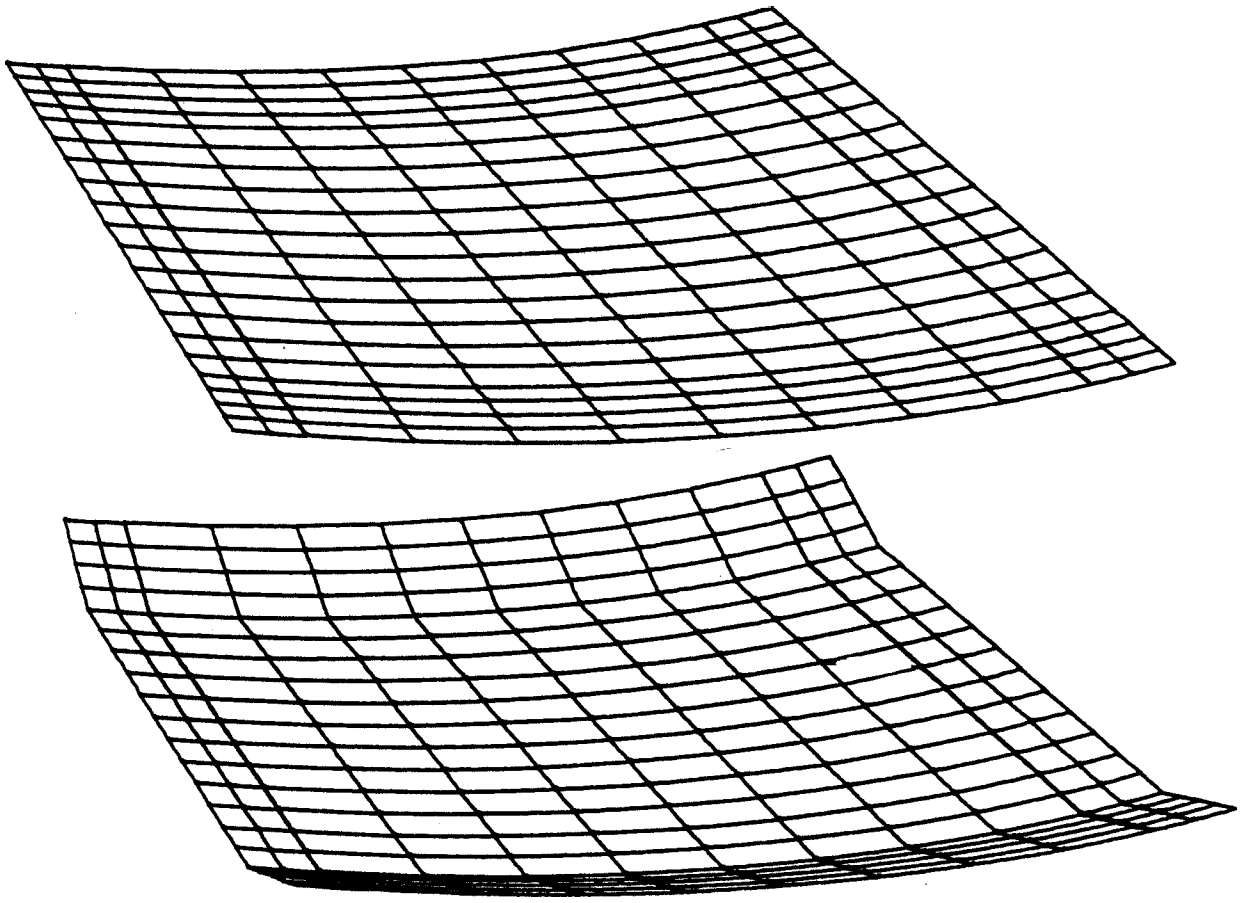

FIGURE 19. Thin Plate Elements for the Coarser Meshed Model, NCURM.

The longitudinal posttensioning was accomplished with the presence of six straight sagged steel truss finite elements, as was done in other models previously. Straight posttensioning longitudinal cables seemed to show more accurate results, as illustrated in the third quarterly report, and hence were used in these models, as opposed to parabolically sagged cables. These cables began at the location corresponding to the top of the voids at the supported end of the slab, and sagged to the bottom of the voids location at the center of the span. Nodal locations along these cables were adjusted vertically within the structural models so that these truss finite elements could be attached. Figure 17 shows a view of these typical truss finite elements for the coarser meshed structural model, NCURM.

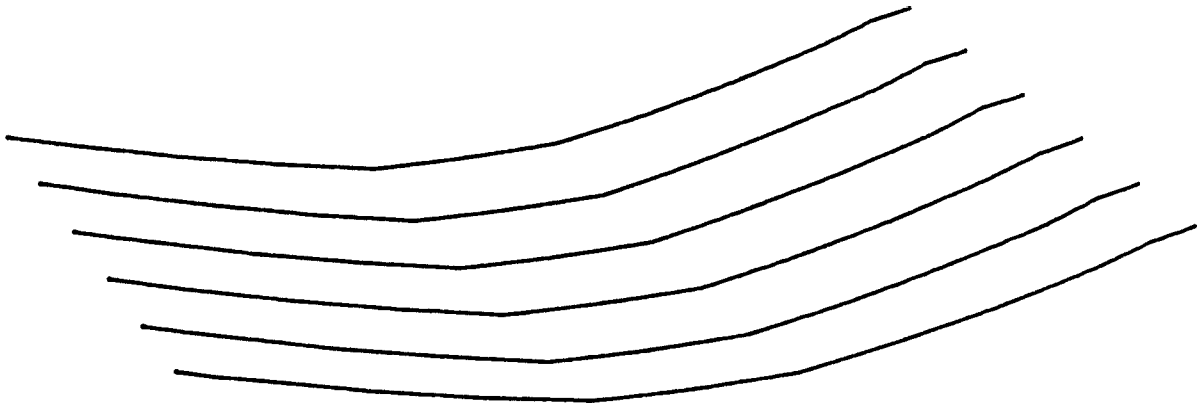

FIGURE 20. Typical Longitudinal Posttensioning Truss Finite Elements, NCURM.

The completed structural finite element model, NCURM, for the coarser meshed model consisted of 1300 node points, 480 thin plate elements, 852 solid elements, and 72 truss elements. The completed structural finite element model, NFCURM, for the finer meshed model consisted of 1904 node points, 768 thin plate elements, 1270 solid elements, and 96 truss elements. The slab was assumed to be made of concrete with an elastic modulus of 3×10^6 pounds per square inch, a Poisson's ratio of 0.15, and a weight density of 0.087 pounds per cubic inch. The steel posttensioning truss elements were arbitrarily assumed to have a cross sectional area of 0.196 square inches (1/2 inch diameter), an elastic modulus of 30×10^6 pounds per square inch, a Poisson's ratio of 0.3, a weight density of 0.283 pounds per cubic inch,. and a coefficient of thermal expansion of 6.5×10^{-6} inches per inch per degree Fahrenheit. Three different static load cases were independently analyzed. These three static load cases were:

1. Gravity loading (dead load);
2. Longitudinal posttensioning;
3. Transverse posttensioning.

Their results, due to the linear analyses, can be superimposed to determine various combinations. The analyses were run on PRIME 850 Microcomputers, with approximately three hours of CPU time required for the coarser mesh model, and approximately five hours of CPU time required for the finer mesh model. The next section will illustratesome of the results of these analyses.

6.2 Results of Curved Voided Slab Analyses

6.2.1 Gravity Loading (Dead Load)

Each of the structural models NCURM and NFCURM was subjected to a one-g downward load. The weight of the truss elements was not included, thus only the concrete elements were active. Table 1 shows a comparison of maximum displacements and top and bottom stresses for this gravity loading of the two models. Figures 18 and 19 show the deformed shape of the top surface for NCURM and NFCURM respectively under gravity loading. These deformations have been amplified by 100 for ease of viewing.

TABLE 1. Comparison of Maximum Displacement and Stress for Gravity Loading.

Model and Location	Downward Maximum Displacement (in.)	Maximum Stress(psi)
NCURM	0.75298	
NFCURM	0.84883	
NCURM, Top, Longitudinal		619.3(Compression)
NFCURM Top, Longitudinal		664. (Compression)
NCURM, Bottom, Longitudinal		731.7(Tension)
NFCURM Bottom, Longitudinal		796.7(Tension)
NCURM, Top, Transverse		435.6(Tension)
NFCURM Top, Transverse		717.7(Tension)
NCURM, Bottom, Transverse		529.6(Compression)
NFCURM Bottom, Transverse		862. (Compression)

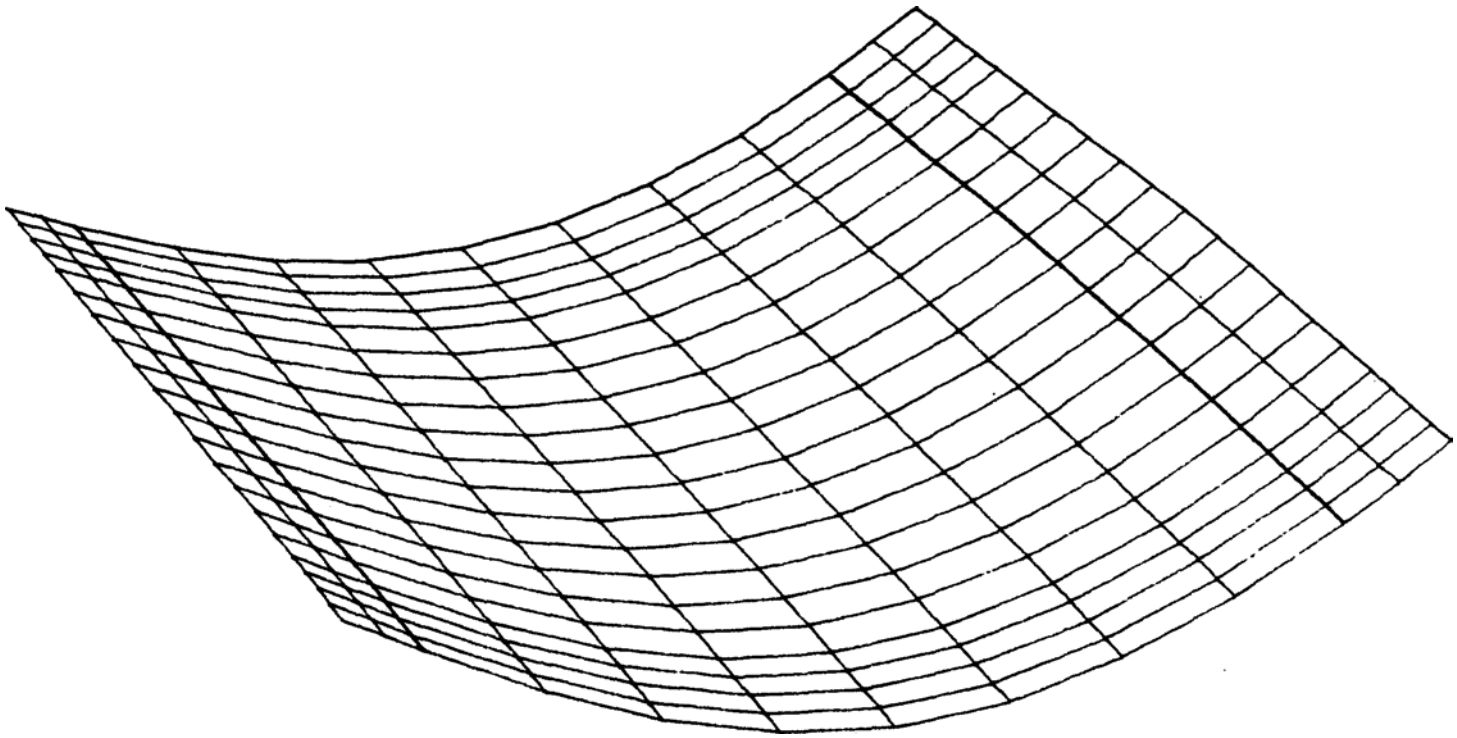

FIGURE 21. Deformation of Top Surface, NCURM, Gravity Loading, Amplified by 100

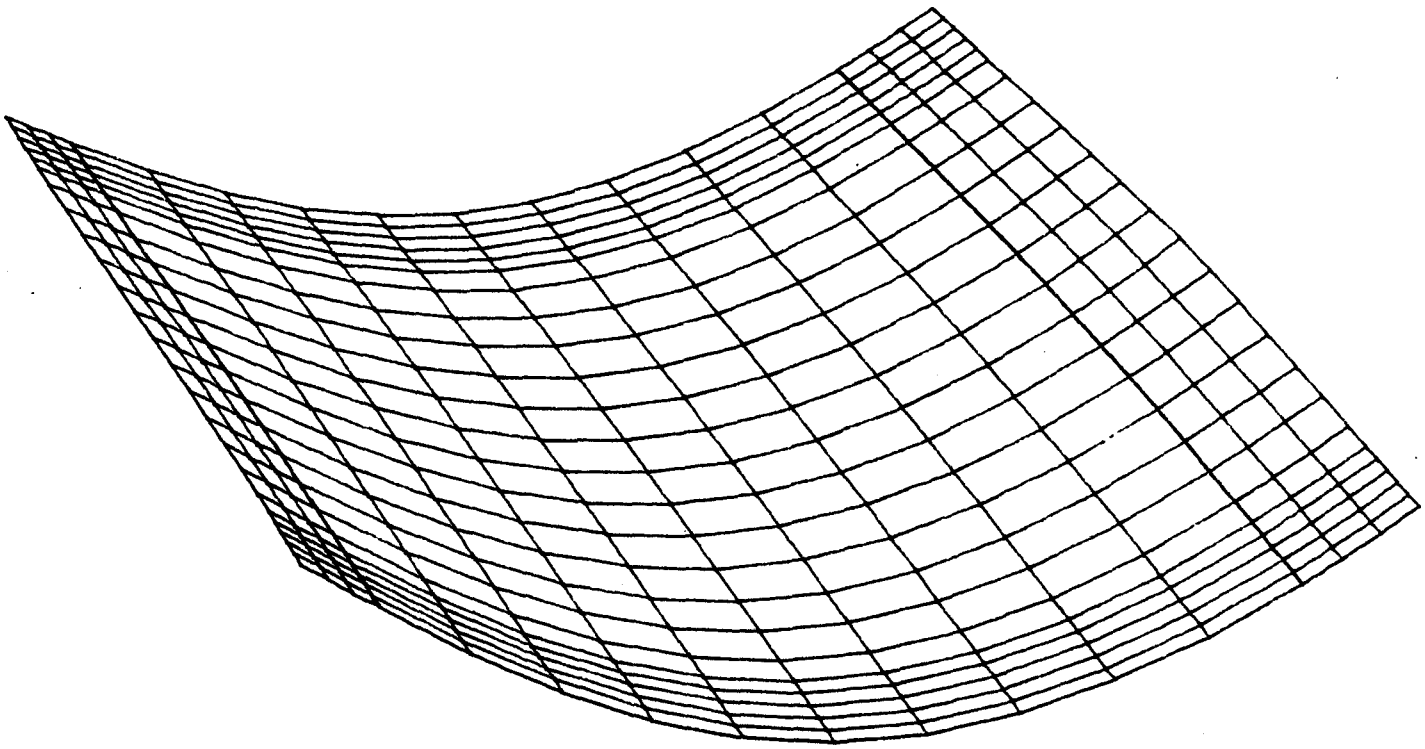

FIGURE 22. Deformation of Top Surface, NFCURM Gravity Loading, Amplified by 100.

Figures 20 and 21 show comparison of longitudinal stress contour plots for the two models for the top and bottom surfaces of the slab respectively. Figures 22 and 23 show comparison of transverse stress contour plots for the two models for the top and bottom surfaces of the slab respectively.

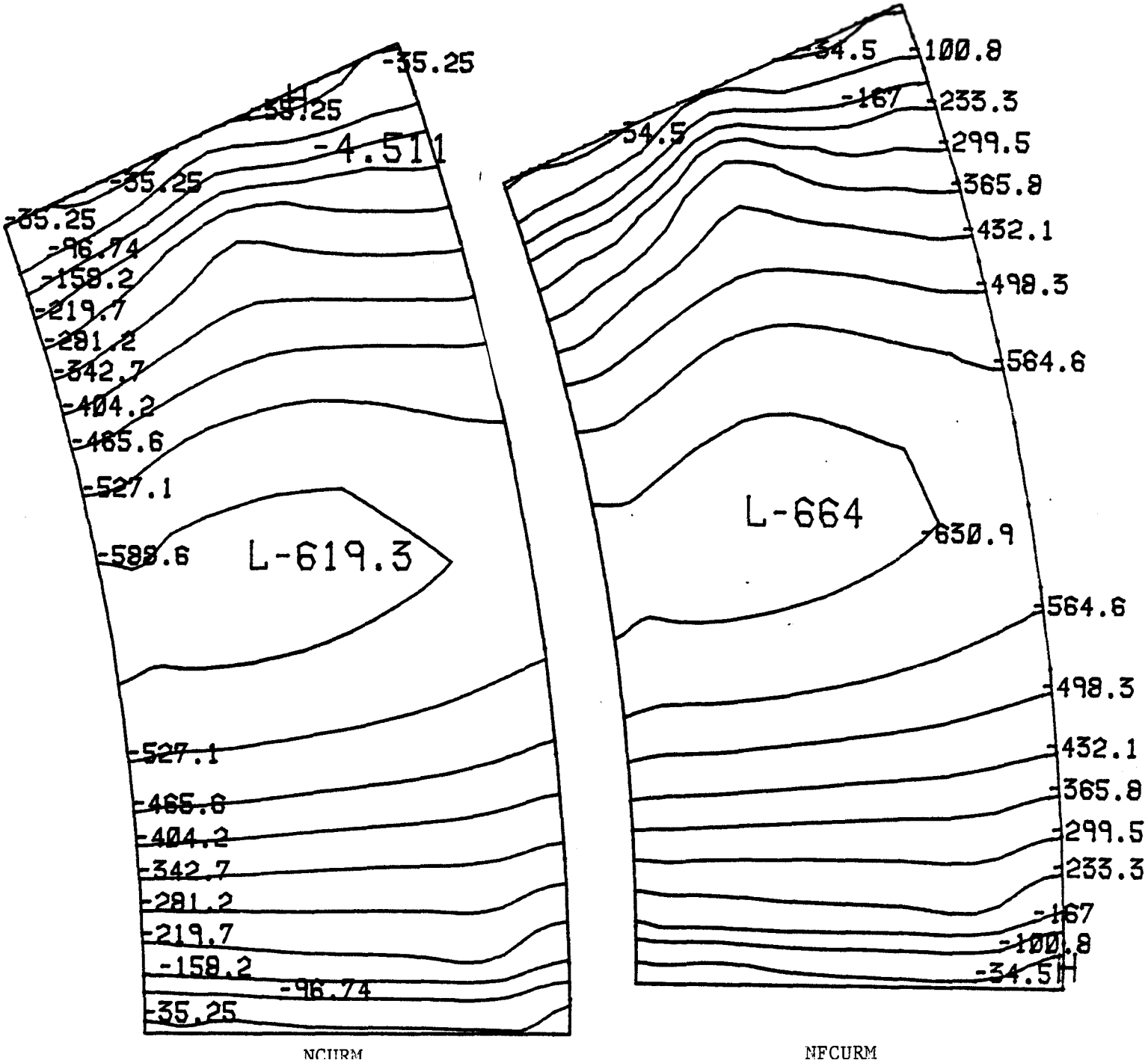

FIGURE 23. Longitudinal Stress Contour Plots Under Gravity Loading, Top

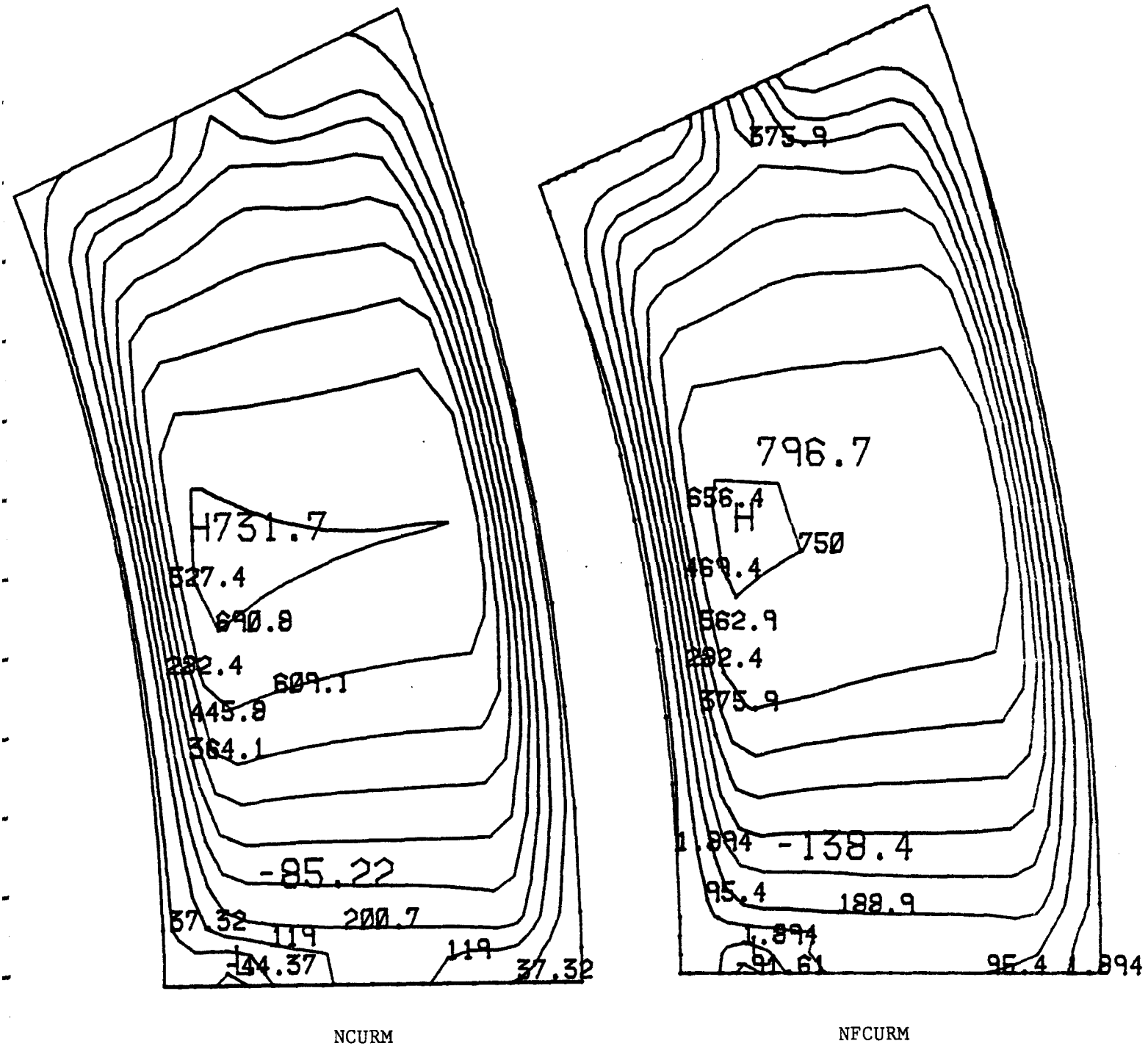

FIGURE 24. Longitudinal Stress Contour Plots Under Gravity Loading, Bottom

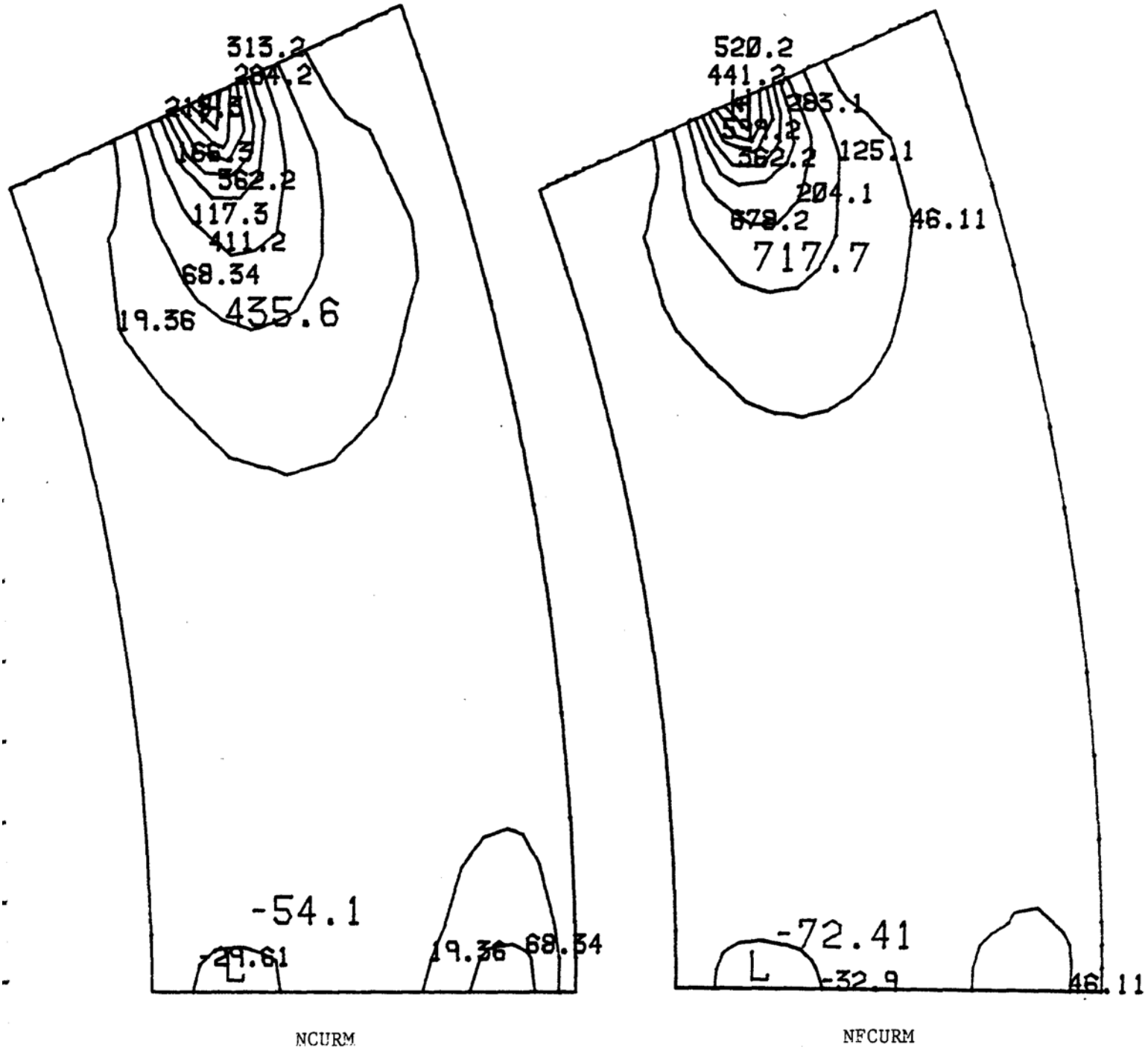

FIGURE 25. Transverse Stress Contour Plots Under Gravity Loading, Top

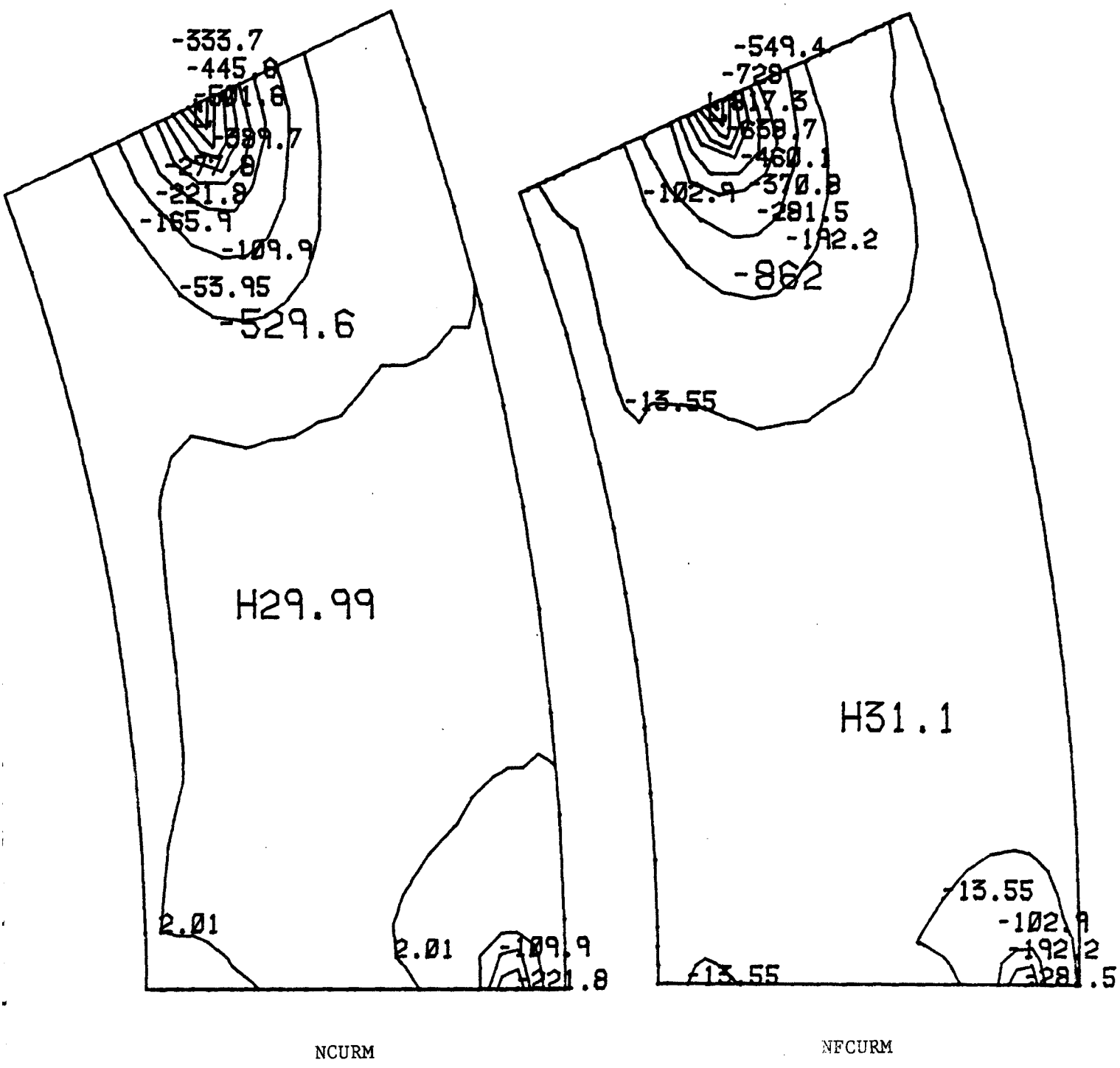

FIGURE 26. Transverse Stress Contour Plots Under Gravitj Loading, Bottom

6.2.2 Longitudinal Posttension Loading

An arbitrary longitudinal posttension force of 3822 pounds was generated in each of the six, one-half inch diameter steel cables by decreasing the temperature in these cables 100^0F. This did not account for any specific friction losses, but as discussed in the second quarterly report, with this modeling scheme there are probably inherent friction losses. Table 2 shows a comparison of maximum displacements and top and bottom stresses for this longitudinal posttension loading for the two models.

TABLE 2. Comparison of Maximum Displacement and Stress For Longitudinal Posttensioning

Model and Location	Upward Maximum Displacement(in)	Maximum Stress (psi)
NCURM	4.4934×10^{-3}	
NFCURM	3.8975×10^{-3}	
NCURM, Top, Longitudinal		3.84 (Tension)
NFCURM Top, Longitudinal		3.743 (Tension)
NCURM, Bottom, Longitudinal		11.35(Compression)
NFCURN, Bottom, Longitudinal		11.34(Compression)
NCURM, Top, Transverse		0.9849 (Tension)
NFCURM Top, Transverse		0.9171 (Tension)
NCURM, Bottom, Transverse		1.955(Compression)
NFCURM Bottom, Transverse		2.731(Compression)

Figures 24 and 25 show the deformed shape of the top surface for NCURM and NFCURM respectively under longitudinal posttensioning. These deformations have been amplified by 11000 for ease of viewing.

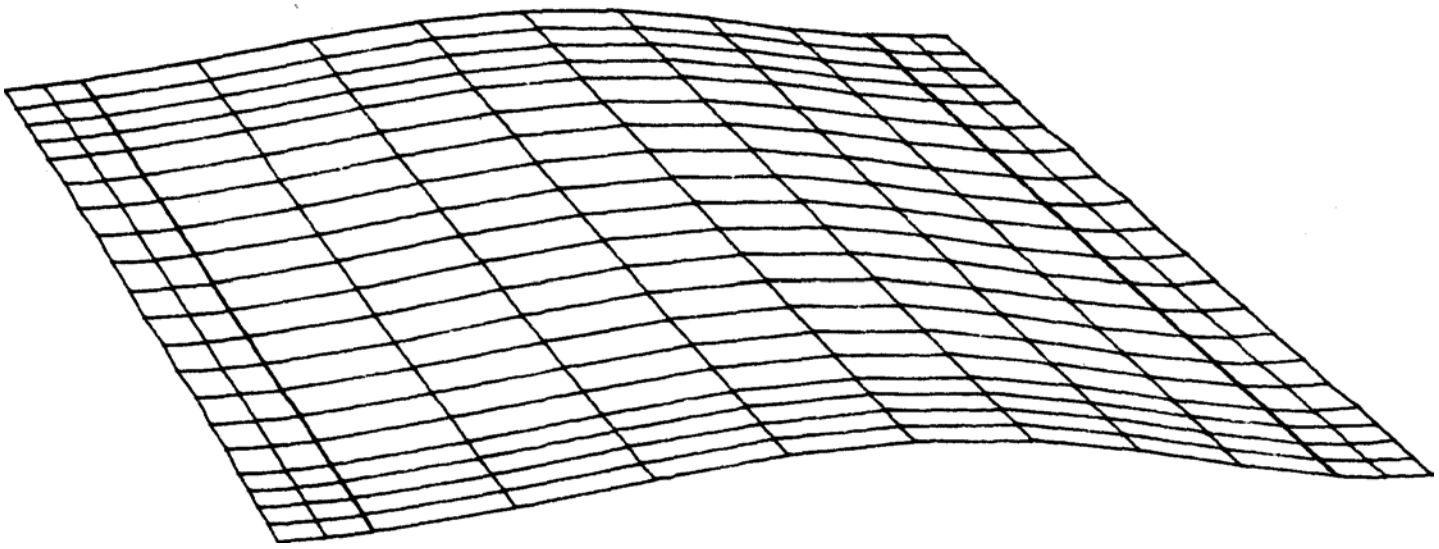

FIGURE 27. Deformation of Top Surface, NCURM, Longitudinal Posttension, Amplified by 11000.

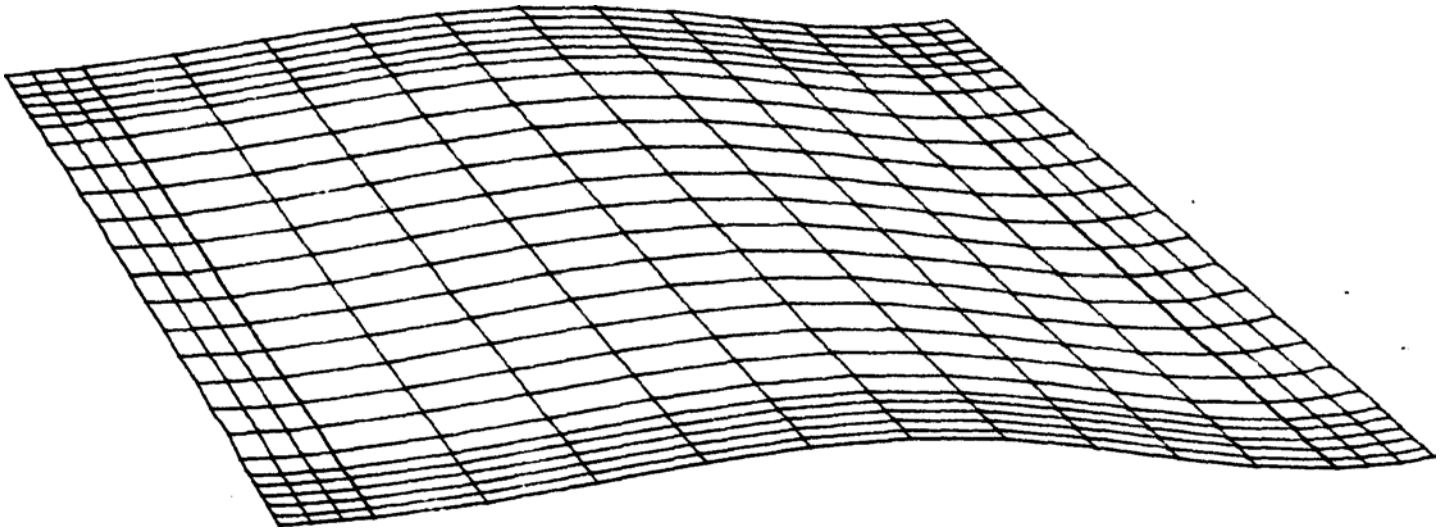

FIGURE 28. Deformation of Top Surface, NFCURM, Longitudinal Posttension, Amplified by 11000.

Figures 26 and 27 show comparison of longitudinal stress contour plots for the two models for the top and bottom surfaces of the slab respectively. Figures 28 and 29 show comparison of transverse stress contour plots for the two models for the top and bottom surfaces of the slab respectively.

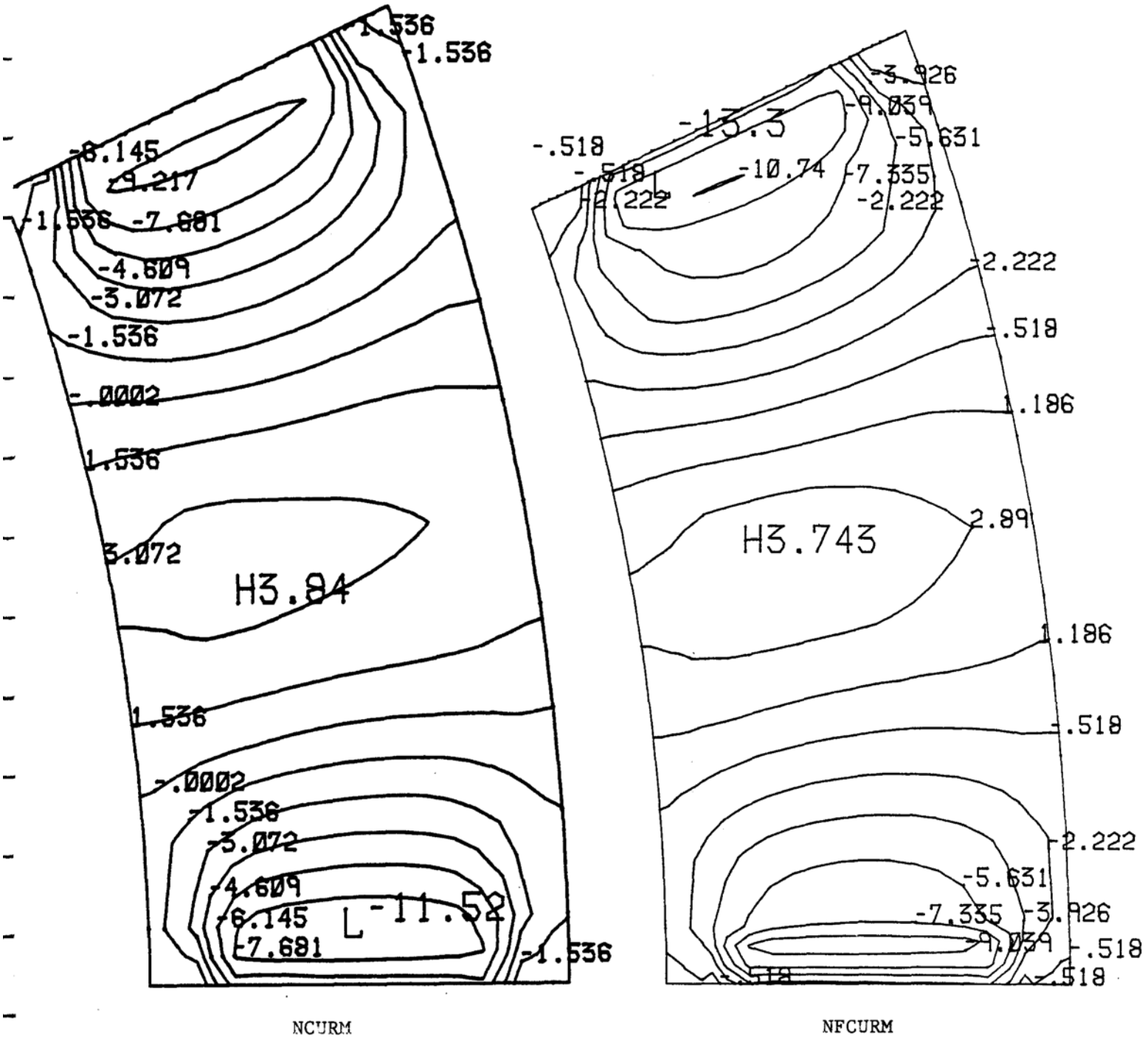

FIGURE 29. Longitudinal Stress Contour Plots Under Longitudinal Posttension, Top.

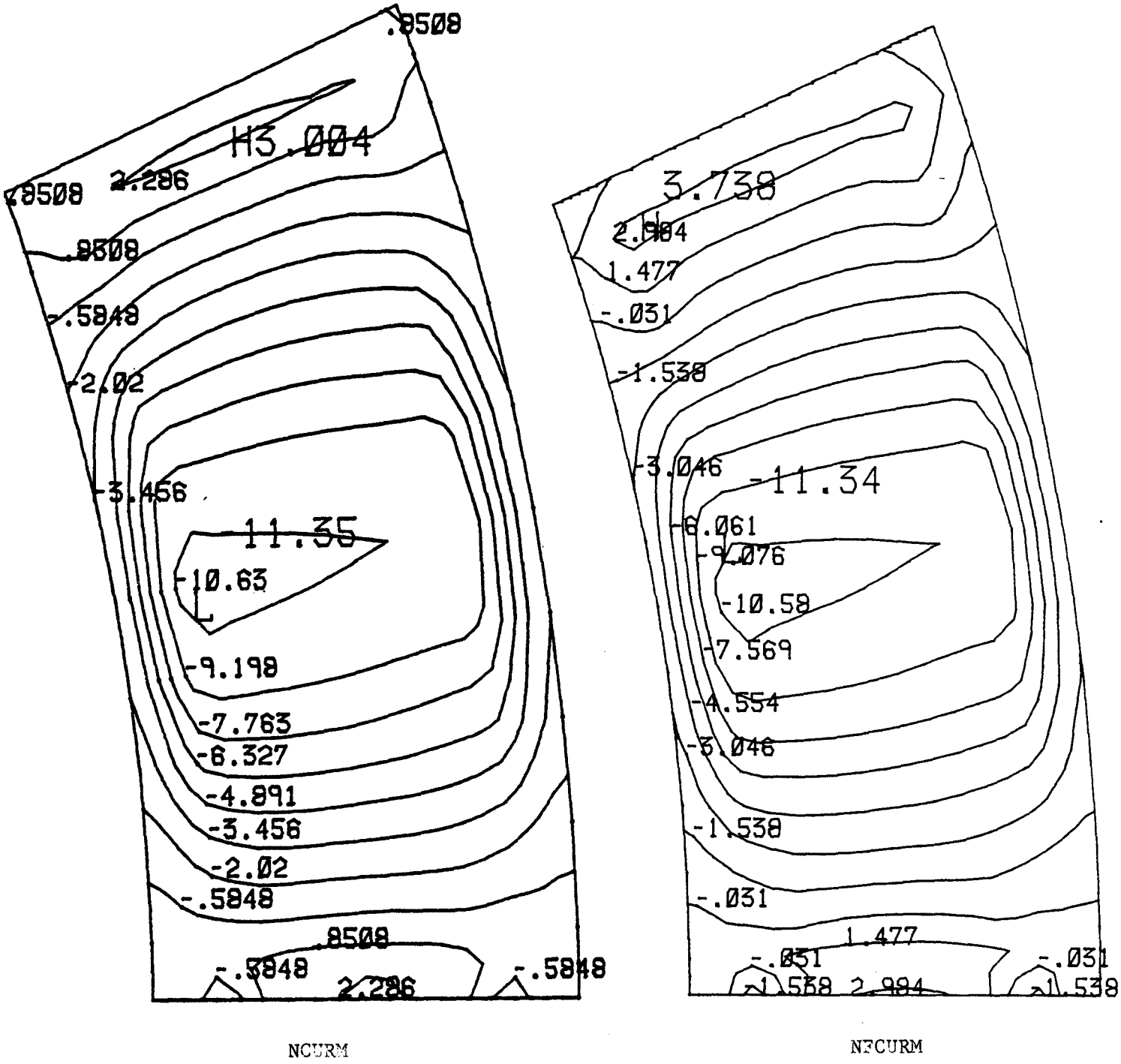

FIGURE 30. Longitudinal Stress Contour Plots Under Longitudinal Posttension, Bottom

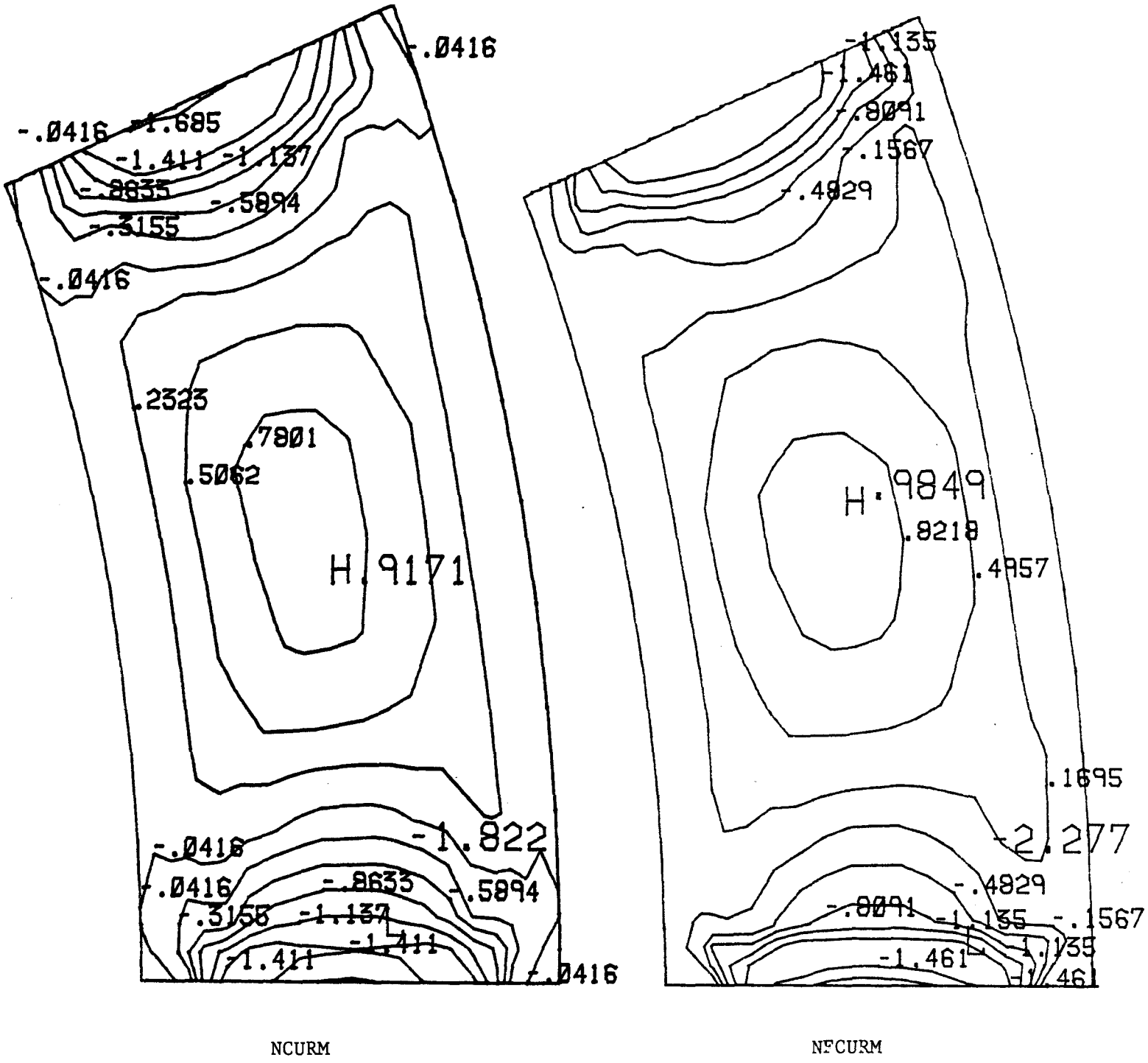

FIGURE 31. Transverse Stress Contour Plots Under Longitudinal Posttension, Top

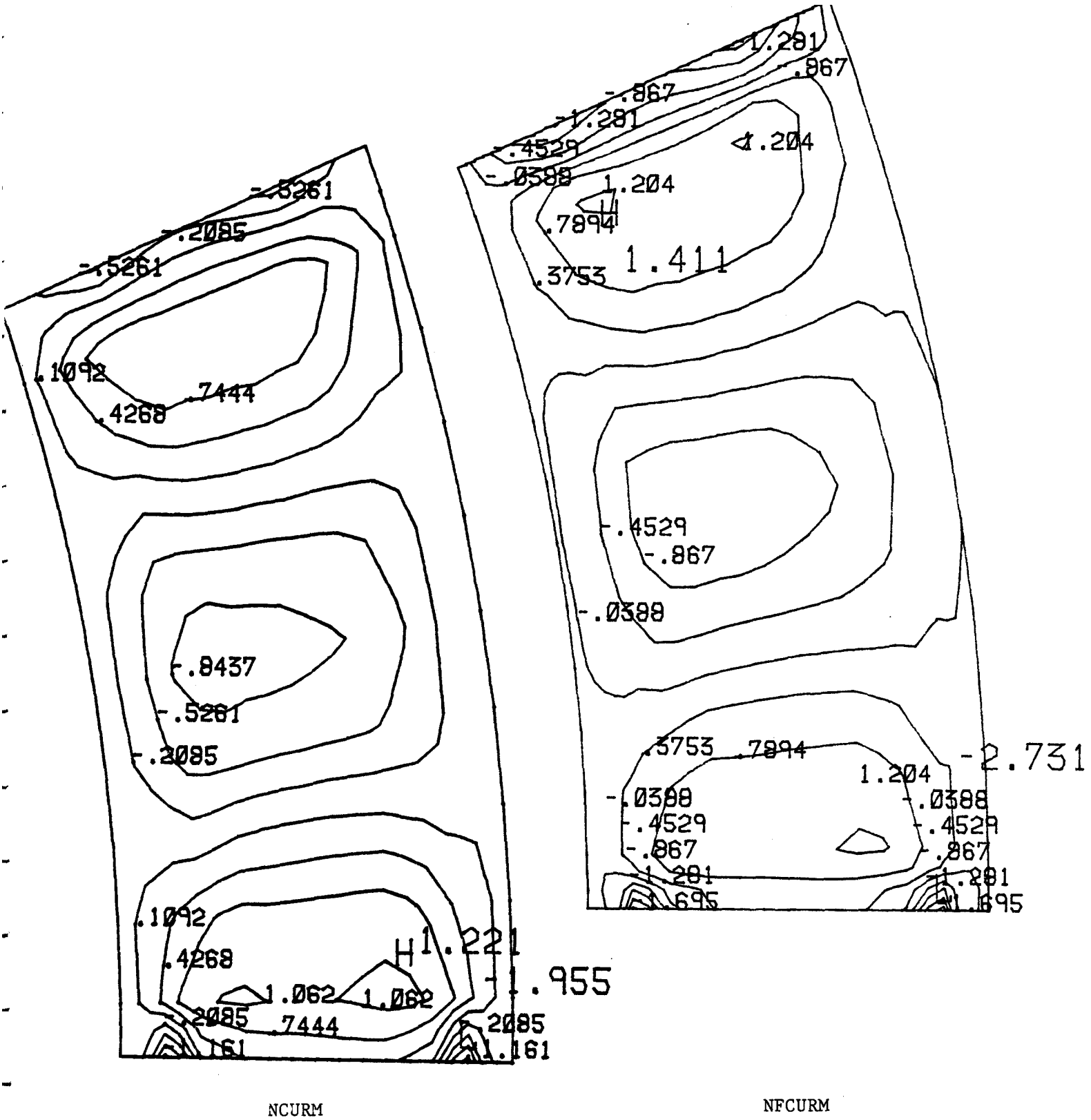

FIGURE 32. Transverse Stress Contour Plots Under Longitudinal Posttension, Bottom

6.2.3 Transverse Posttension Loading

An arbitrary transverse posttension force of 100 pounds was applied to the slab at each division line between elements around the curve. This was simulated by applying 100 pound loads radially outward on the inner radius, and 100 pound loads radially inward on the outer radius at mid depth. Table 3 shows a comparison of maximum displacements and top and bottom stresses for this transverse posttension loading for the two models.

TABLE 3. Comparison of Maximum Displacement and Stress for Transverse Posttensioning

Model and Location	Upward Maximum Displacement(in.)	Maximum Stress (psi)
NCURM	4.5191×10^{-5}	
NFCURM	6.0175×10^{-5}	
NCURM, Top, Longitudinal		0.0513(Compression)
NFCURM Top, Longitudinal		0.0775(Compression)
NCURM, Bottom, Longitudinal		0.106 (Tension)
NFCURN, Bottom, Longitudinal		0.4913 (Tension)
NCURM, Top, Transverse		0.9599(Compression)
NFCURM Top, Transverse		1.246(Compression)
NCURM, Bottom, Transverse		0.1481(Tension)
NFCURM Bottom, Transverse		0.2329 (Tension)

Figures 30 and 31 show the deformed shape of the top surface for NCURM and NFCURM respectively under transverse posttensioning. Deformations have been amplified by 800,000 for ease of viewing.

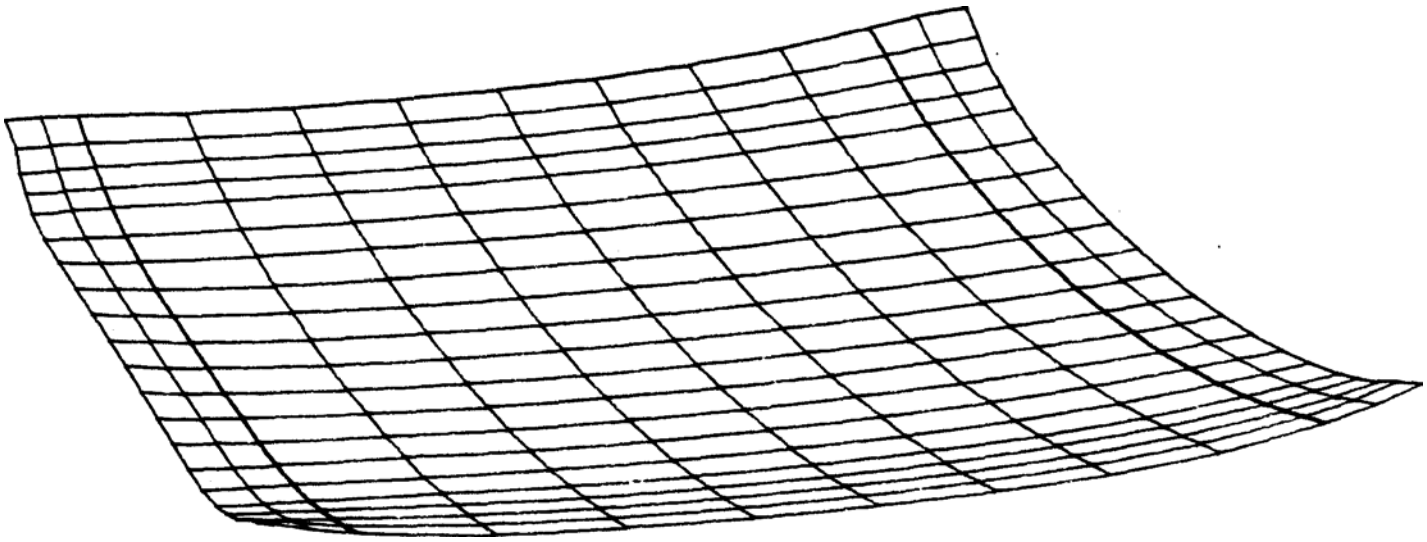

FIGURE 33. Deformation of Top Surface, NCURM, Transverse Posttension, Amplified by 800,000.

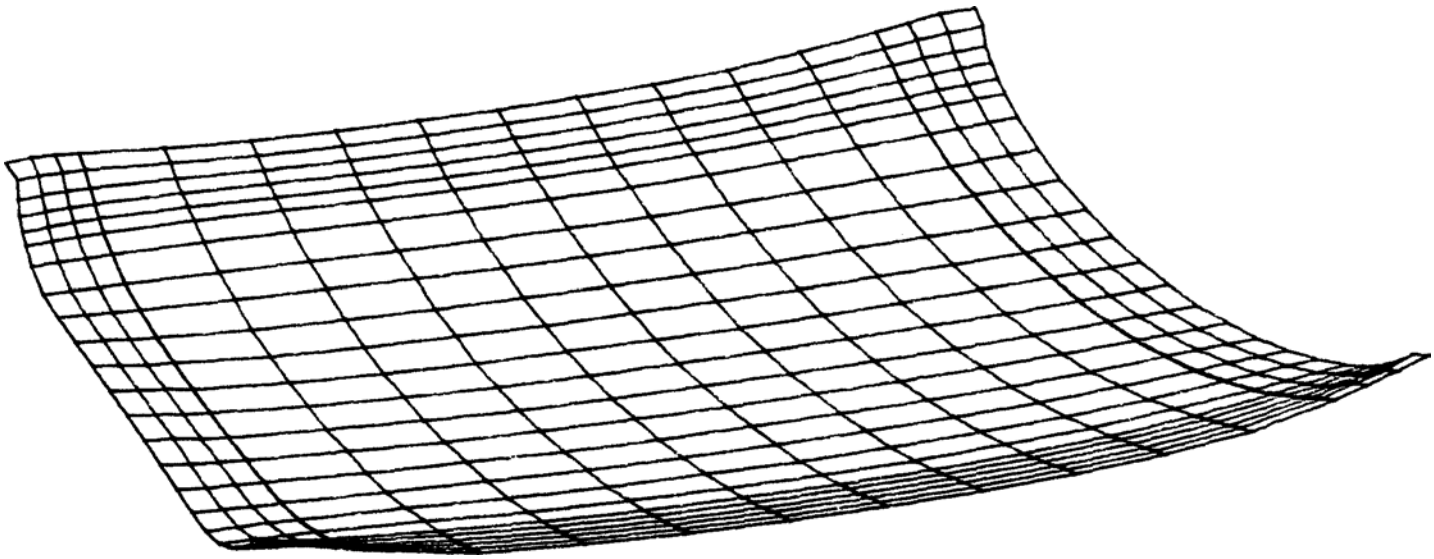

FIGURE 34. Deformation of Top Surface, NFCURM, Transverse Posttension, Amplified by 800,000.

Figures 32 and 33 show comparison of longitudinal stress contour plots for the two models for the top and bottom surfaces of the slab respectively. Figures 34 and 35 show comparison of transverse stress contour plots for the two models for the top and bottom surfaces of the slab respectively.

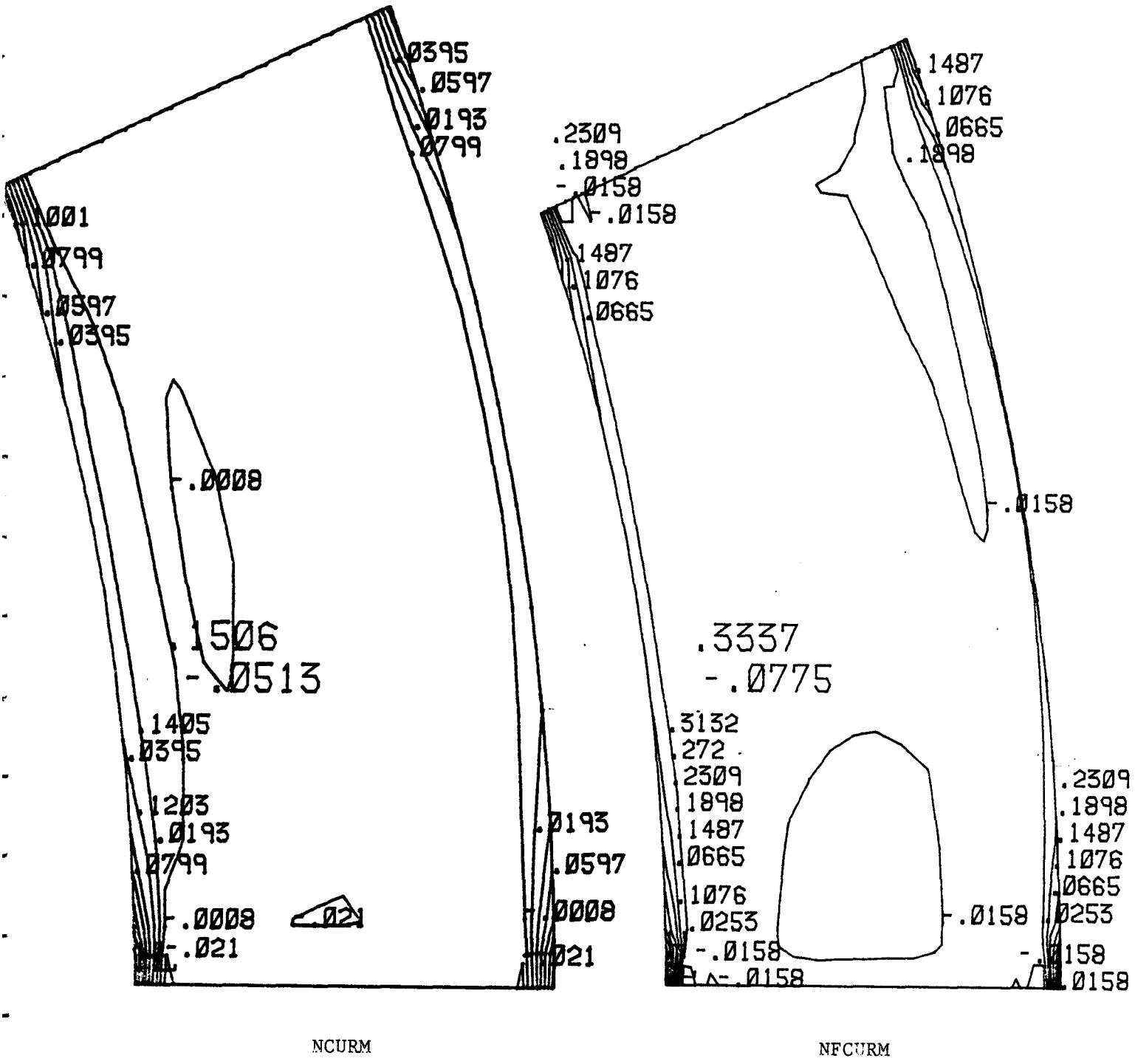

NCURM NFCURM

FIGURE 3.5. Longitudinal Stress Contour Plots Under Transverse Posttension, Top.

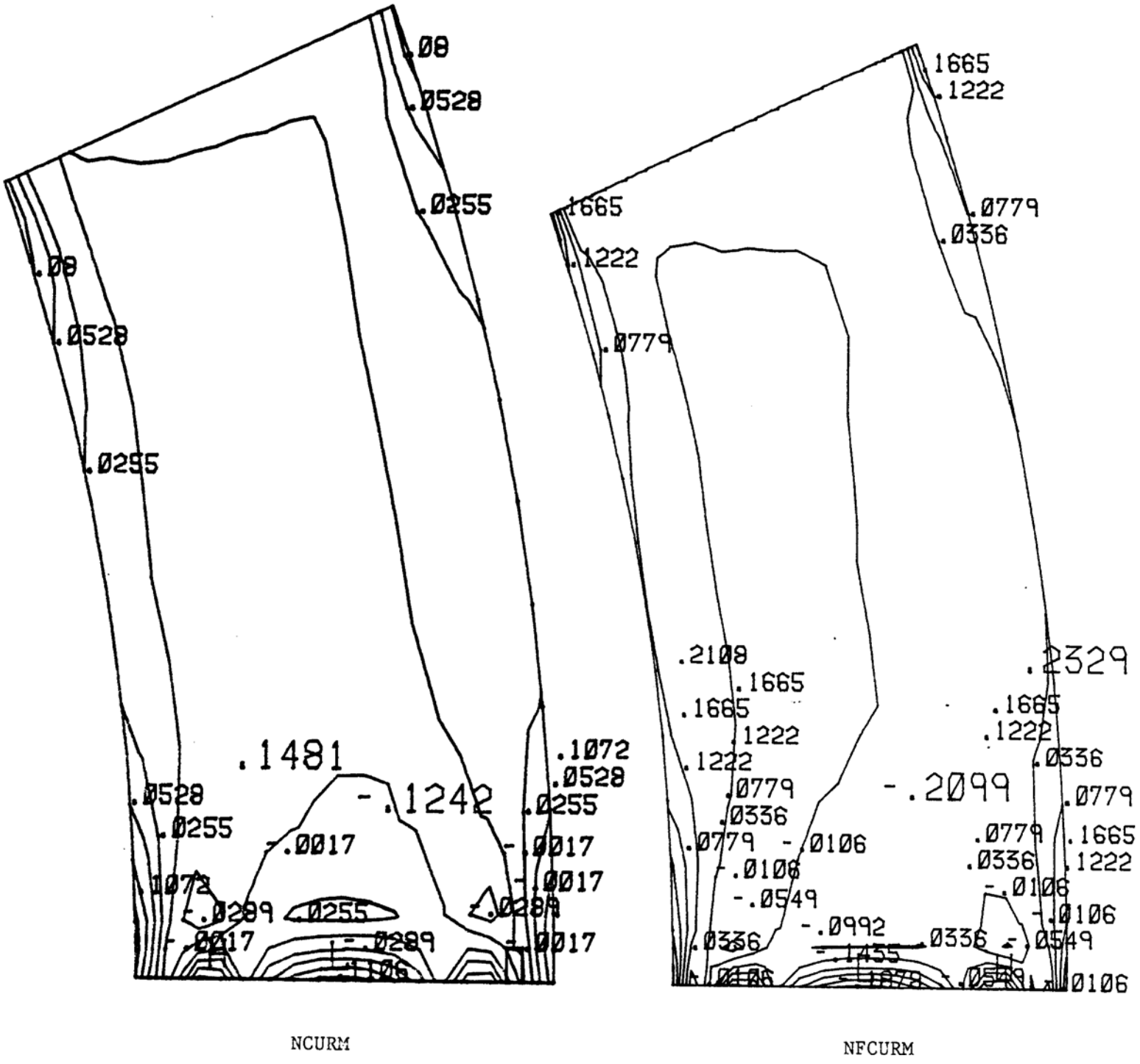

FIGURE 36. Longitudinal Stress Contour Plots Under Transverse Posttension, Bottom

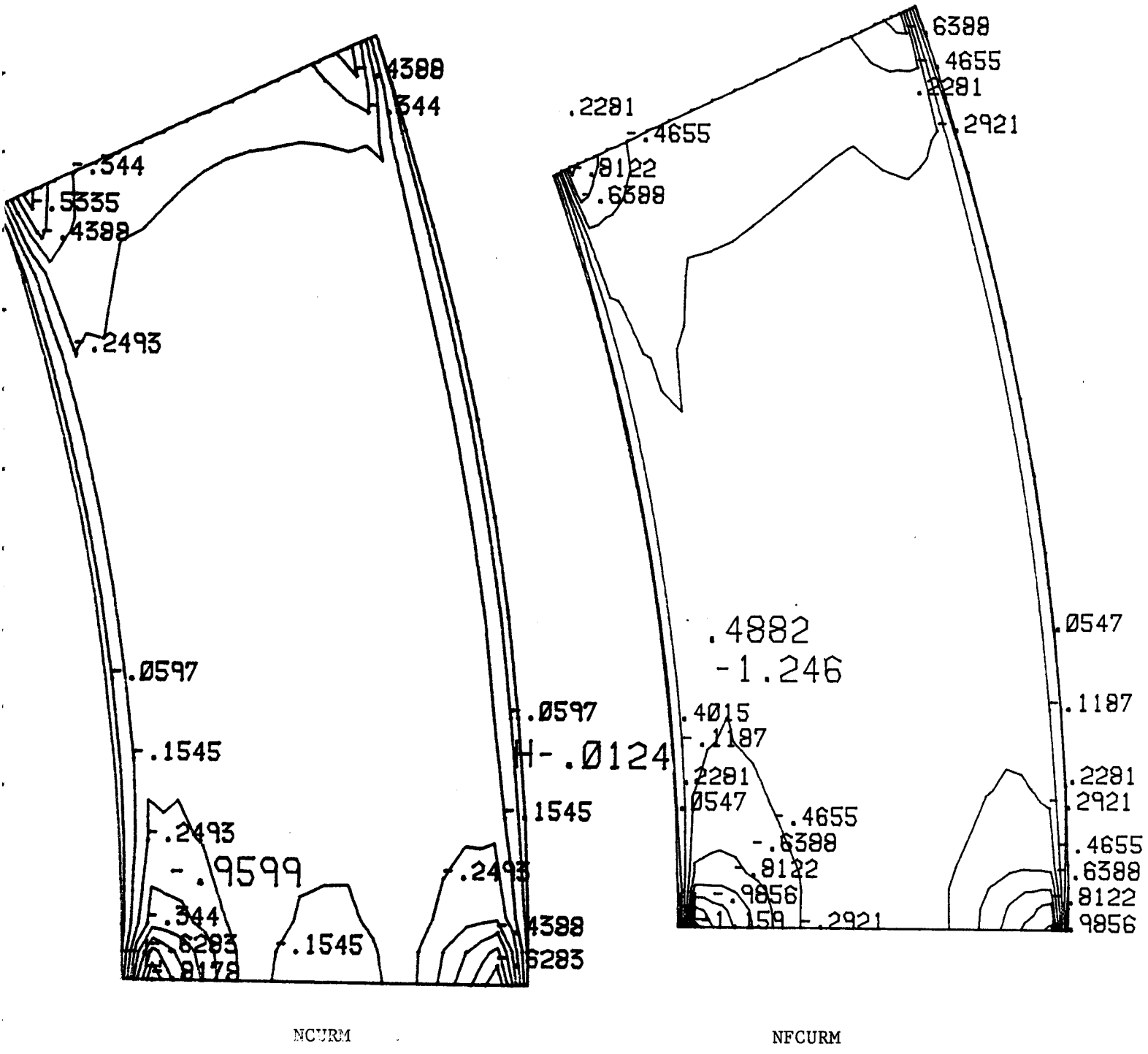

FIGURE 37. Transverse Stress Contour Plots Under Transverse Posttension, Top.

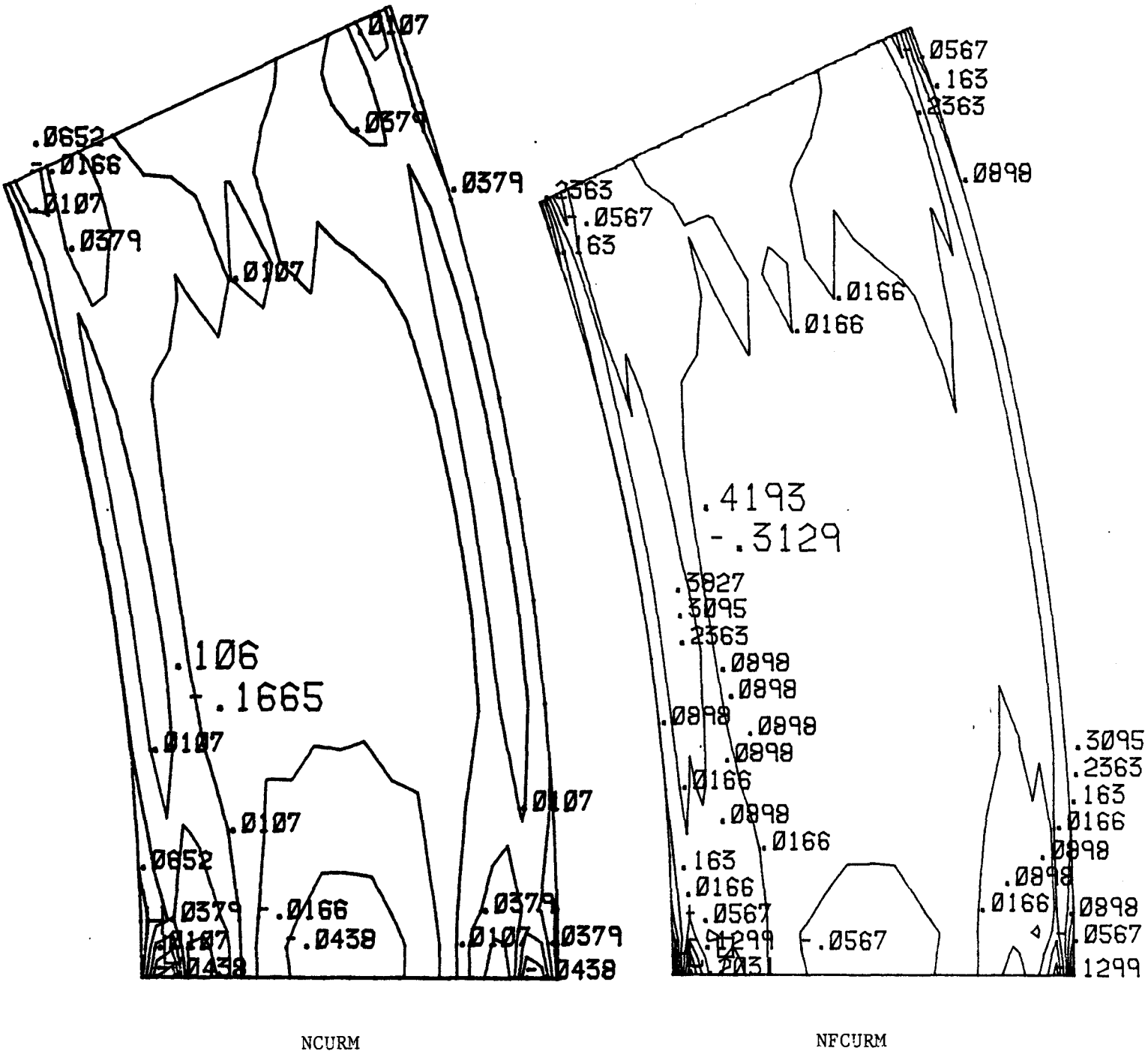

NCURM NFCURM

FIGURE 38. Transverse Stress Contour Plots Under Transverse Posttension, Bottom

6.3 Discussion of Results

The comparative results shown in Tables 1, 2, and 3, for the coarser meshed model, NCURM, and the finer meshed model, NFCURM, illustrate that maximum displacements and stresses are in good agreement. The finer meshed model results should be viewed as more accurately determining the response of the structure to the three static load cases.

As can be seen from Table 1, less deflection and tensile stress were produced by gravity loading for this model (possessing 33% voids) than the previous curved voided span model considered in the third quarterly report (11.5% voids). Maximum deflections downward due to gravity loading were reduced from 1.363 inches to 0.84883 inches. Maximum longitudinal tensile stresses on the bottom surface of the slab were reduced from 1019pounds per square inch to 796.7 pounds per square inch.

As can be seen from Table 2, more deflection and compressive stress were produced from the same longitudinal posttension loading than the previous curved voided span model. Due to longitudinal posttensioning the maximum upward deflection increased from 5.281×10^{-5} inches to 3.8975×10^{-3} inches. The maximum longitudinal compressive stress on the bottom surface of the slab increased from 9.125 pounds per square inch to 11.34 pounds per square inch. The net effect of these model changes means that, with the 33% void model, in order for the longitudinal posttension load to overcome the effect of gravity, longitudinal posttension loads of 268,517 pounds are necessary. The previous 11.5% void model required a longitudinal posttension

load of 426,807 pounds to overcome the gravitational load.

The effects of transverse posttensioning did not vary much from the 11.5% void model to the 33% void model, which illustrates that transverse stiffness is still present in the 33% void model. Figures 20 and 26 show that longitudinal stress contours due to gravity and longitudinal posttension loading on the top surface of the voided slab behave somewhat like one would expect of a straight beam under bending. If it were truly a straight beam then the stress contour lines would be practically uniform from side to side. However, in the curved slab situation the longitudinal stresses seem to maximize on the inside radius of the' slab, and then decrease toward the outer radius of the slab. As the radius of the slab is decreased this variation of longitudinal stress from inside to outside would be more pronounced. This same behavior is somewhat exhibited on the bottom surface of the slab, discounting the flange areas, and shown in Figures 21 and 27.

Calculations were conducted on the voided cross section and solid cross section (near the supports) to determine their area, A; their position of the neutral axis from the bottom surface of the slab, Z_{NA}; second moments of area about the horizontal (I_y) and vertical (I_Z) neutral axes of the cross section; and the torsional constants, J, of the cross sections. These calculations revealed that

Voidet Cross Section		SolidCross Section	
A	= 6062.77 in.^{2}	A	=9048.06 in.^{2}
Z_{NA}	= 17.26 in.	Z_{NA}	=16. 79 in.
I_y	= 612274.1 in.^{4}	I_y	=725664.3 in.^{4}
I_Z	= 49730269.8 in.^{4}	I_Z	=63728202.6 in.^{4}
J	= 1773182.7 in-^{4}	J	=2599974.6 in.^{4}

Using these cross section parameters, and noticing the values of the longitudinal stresses on the top and bottom of the slab from Table 1 for gravity loading, the ratio of these stresses (top to bottom) should be in the same ratio as distances from the neutral axis to the top and bottom surfaces. This ratio for the voided section is given by

$$(31.67 - 17.26)/17.26 = 0.8349$$

and the ratio of stresses for model NFCURM from Table 1 is 664/796.7 = 0.8334

which is quite close.

A computer analysis; using beam elements with cross section properties just illustrated to represent the curved voided slab structure, with the same material properties, gravity loading, and simple supports; was conducted. A comparison of the results with Table 1 is shown in Table 4.

Table 4. Comparison of Curved Beam Results with NFCURM for Gravity Loading.

ITEM	Curved Beam	NFCURM
Maximum Deflection	0.522 in.	0.84883 in.
Max. Long. Stress, Top	576.7 psi	664. psi
Max. Long. Stress, Bottom	690.7 psi	796.7 psi

It should be pointed out that the maximum deflection for the curved beam analysis is at the center of the slab, whereas the

maximum deflection for the voided slab model (NFCURM) is on the outside of the slab, where the deflection is more than the center of the slab (approximately another 0.15 inches more). Thus, there exists approximately 15 to 20% error between these models. The voided slab model, NFCURM, however gives more conservative (i.e. on the high side) results.

9. REFERENCES

1. Standard Specifications for Highway Bridges, AASHTO, 13th Edition, Washington, D.C., 1983.

2. ACI Committee 318, "Building Code Requirements for Reinforced Concrete (ACI 318-86R)", American Concrete Institute, Detroit, 1986.

3. Ontario Highway Bridge Design Code, 2nd Edition, 1983. Ministry of Transportation and Communications, Downsview, Ontario, Canada. 4. Elliot, G. and Clark, L.A., "Circular Voided Concrete Slab Stiffness. Journal of the Structural Division, ASCE, Vol 108, November 1982, pp. 2379-2393.

5. Bishara, A., "Prestressed concrete beams under combined torsion, bending and shear", ACI Journal, Vol 66, No 7, July 1969, pp. 525538.

6. Henry, R.L. and Zia, P., "Prestressed beams under torsion, shear and bending", Journal of the Structural Division, ASCE, Vol 100, May 1974, pp. 933-952.

7. Mukherjee, P.R. and Warwaruk, J., "Torsion, bending and shear in prestressed concrete", Journal of the Structural Division, ASCE, Vol 97, April 1971, pp. 1063-1079.

8. McMullen, A.E. and Woodhead, H.R., "Experimental study of prestressed concrete under combined torsion, bending and shear", PCI Journal, Vol 18, No 5, September-October 1973, pp. 85-100..

9. BIAXM - Program for the determination of the ultimate moment capacity of prestressed concrete sections under biaxial stress. D. Hodge, USF, 1987.

10. Lee, E.Y.K. "Behavior of curved, continuous prestressed concrete beams loaded to collapse", Thesis submitted to Queen's University, Kingston, for degree of M.Sc, June 1978, pp. 135.

11. Cohn, M.Z. and Frostig, Y. "Inelastic behavior of continuous prestressed concrete beams", Journal of Structural Engineering, ASCE, Vol 109, No 10, October 1983, pp. 2292-2309.

12. Hodge, D. "Strength of longitudinally and transversely prestressed concrete beams under bending, shear and torsion". Thesis to be submitted to the University of South Florida, January 1988.

13. Zia, P. and McGee, W.D. "Torsion design of prestressed concrete", PCI Journal, Vol 19,'No 2, March-April 1974, pp. 47-65.

14. Jaeger, L. and Bakht, B. Private communication, September 1987.